Fingering phenomena for driven coating films

M. H. Eres, L. W. Schwartz, and R. V. Roy
Department of Mechanical Engineering, University of Delaware, Newark, Delaware 19716

(Received 9 September 1999; accepted 28 February 2000)

A theoretical and numerical model is formulated to describe the instability and the long-time evolution of both gravity-driven and surface-shear-stress-driven thin coating films. A single evolution equation, of higher-order diffusive type, models the flow for either problem. It is derived using the lubrication approximation. For partially wetting systems, the effect of finite contact angle is incorporated in the equation using a particular disjoining pressure model. The base state, in each case, is a two-dimensional steadily propagating capillary front. Slight perturbations of the base state, applied along the front, initiate the fingering instability. Early-time results accurately reproduce the wavelengths of fastest growth and the corresponding eigenmodes as reported in published linear stability analyses. As time proceeds, depending on parameter values, various fingering patterns arise. For conditions of perfect wetting with the substrate downstream of the moving front covered with a thin precursor layer, predicted nonlinear finger evolution agrees well with published experiments. The ultimate pattern, in this case, is a steadily translating pattern of wedge-shaped fingers. Alternatively, for partially wetting systems that exhibit sufficiently large static contact angles, long straight-sided fingers or rivulets are formed. Finally, for larger contact angles, or at relatively low speeds, we predict that the flowing rivulets will become unstable and break up into strings of isolated droplets. © *2000 American Institute of Physics.* [S1070-6631(00)00506-7]

I. INTRODUCTION

We are concerned here with the slow flow of thin liquid layers on a solid surface or substrate. The flow is driven by body forces, surface tractions, or a combination of these. A wet coating of paint that is applied to a vertical wall will flow downward until the paint has dried; in the coatings industry this phenomenon is called ''sagging.'' If the paint layer is of nonuniform thickness, with a thicker region lying above a thin region, a relatively steep front can develop as the paint flows downward. Often this front will develop undulations that lead to growing ''fingers'' of paint. Such unsightly ''drip marks'' in the final dry coating can be a serious problem, particularly if the coating serves a decorative purpose. Nonuniformity in the thickness of downward flowing liquid layers is also a concern in chemical and nuclear reactors where the liquid may be used to thermally protect the reactor walls, or, in certain chemical reactors, where liquid–gas contact is necessary for chemical interaction between the phases.[1,2]

Driven liquid films, which develop steep fronts leading to finger growth, also occur when flow is produced by centrifugal force or a surface traction caused by wind blowing essentially parallel to the film. Both these cases were treated experimentally by Tanner.[3] Because surface tension σ is a monotonically decreasing function of temperature for common liquids, a surface shear stress can also result from a temperature gradient along the film that produces a surface tension gradient. To the extent that the temperature can be made to vary linearly along the substrate and the thin adjacent film, and provided that the total temperature difference is small, the surface stress, or traction, given by

$$\boldsymbol{\tau} = \nabla \sigma,$$

is essentially constant. Flows produced by temperature-induced surface tension gradients are often termed Marangoni flows. Climbing Marangoni films on a vertical differentially heated plate, partially submerged in a liquid bath, were demonstrated by Ludviksson and Lightfoot.[4] More recently Cazabat *et al.*[5] demonstrated that these rising fronts can be unstable, resulting in evolving fingering patterns. These fingers were photographed using interferometry.

A climbing film on a vertical plate is shown schematically in Fig. 1(a). Using the lubrication approximation and asymptotic matching to a static meniscus at the bath, the rising film thickness can be calculated (region I of the figure).[6,7] In region II the film thickness h_∞ is virtually constant and the length of the region grows with time. Gravity drainage in this region is negligible for sufficiently thin films, specifically when $\rho g h_\infty \ll \tau$. Here ρ is the liquid density. The analysis leading to the prediction of h_∞ closely parallels the Landau–Levich analysis for the thickness of the liquid film on a plate that is drawn vertically from a bath at constant speed.[8] For the rising stress-driven film, the result is

$$h_\infty = C\left(\frac{\sigma}{\rho g}\right)^{3/2}\left(\frac{\tau}{\sigma}\right)^2, \tag{1}$$

where C is an order-one pure number that is found by numerical integration of the third-order ordinary differential equation satisfied by the film thickness variation in region I. The value of C is $4.8051\ldots$, about 1% smaller than the value calculated by Fanton *et al.*[7] As discussed further in Sec. II B, gravitational backflow may be neglected in the thin climbing film, provided the dimensionless group $\tau/\sqrt{\rho g \sigma}$,

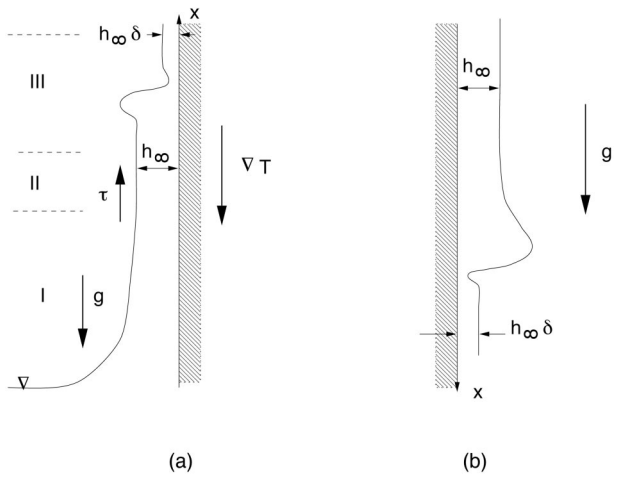

FIG. 1. Schematic of (a) surface-tension-gradient-driven climbing film on a vertical wall where the wall temperature decreases in the upward direction and (b) film draining due to gravity. In both cases the front moves onto a prewetted substrate with film thickness $h_\infty \delta$. These figures are not drawn to scale; in particular the prewetted thickness dimension is greatly exaggerated.

formed from the input parameters, is sufficiently small. In this case, gravity only enters the problem via the radius of curvature of the essentially static meniscus which is proportional to $\sqrt{\sigma/(\rho g)}$.

This paper considers the fate of the propagating front shown in region III of Fig. 1(a). When gravity-driven backward drainage is neglected, the simplified problem is identical to that produced by a constant wind shear stress on the free surface. The problem is also qualitatively similar to the behavior of a front propagating downward due to the action of gravity alone, as shown in Fig. 1(b). In each case, the idealized problem has a uniform ''thick'' film of thickness h_∞ in the far field, i.e., as $\tilde{x} \to -\infty$. Also, in each case, the front is preceded by a thin uniform wetting layer of relative thickness $\delta \ll 1$ as $\tilde{x} \to +\infty$. The role of this thin layer will be explained below.

Each of these idealized problems possesses a steady-state or *base state* solution in a moving coordinate system that, for certain parameter ranges, is unstable. The speed of propagation for each steadily translating solution is essentially determined by upstream conditions when δ is small, as discussed in the next section. Each problem, when suitably nondimensionalized, has a one-parameter family of solutions, corresponding to different values of δ. As $\delta \to 0$, the mound height, just upstream of the front, becomes large in order to overcome the large viscous resistive force in this limit. Because the no-slip condition is applied on the substrate, this is a singular limit, corresponding to the theoretical impossibility of moving a ''contact line'' on a dry surface.[9] These base-state solutions satisfy related third-order nonlinear differential equations and can be found conveniently by using a ''shooting'' method. The procedure is developed in Tuck and Schwartz[10] for the gravity drainage problem and has recently been extended to the Marangoni problem by Kataoka and Troian.[11]

Stability analyses of the base states confirm that each problem is unstable and, when perturbed, will display growing periodic fingers. Numerical solutions of the linear stability problem have identified the fastest growing eigenmodes in each case.[11,12]

While the Marangoni-stress-driven experiments of Cazabat *et al.*[5,13] possess a steady two-dimensional base state, available gravity drainage experiments do not have this property. Several experimental studies report on gravity drainage on inclined plane substrates where a volume of liquid is initially confined behind a ''dam.'' [14–16] At the start of the experiment the dam is removed and the liquid mound flows down the incline. Since the liquid volume is constant, the average coating thickness decreases as the mound spreads downhill. There is no constant source of liquid supply as in the model problem of Fig. 1(b). These drainage experiments do exhibit fingering and also reveal how fingering is affected by the equilibrium contact angle θ_e that the liquid makes with the substrate material. Silvi and Dussan,[15] for example, used glycerine on both glass (good wetting, small θ_e) and plastic substrates (poor wetting, large θ_e). For the glass substrate case, the formed fingers were wedge shaped and finger lengths were limited. On the plastic substrate, on the other hand, fingers were observed to be essentially straight-sided and appeared to lengthen indefinitely. A finite-difference simulation of the low-contact-angle case, using a lubrication-theory model, was reported by us some time ago.[17]

Another type of experiment that has many of the features of the present problem, including a steady two-dimensional base state and downhill precursor layer of liquid, is the so-called rimming experiment.[18,19] A small quantity of liquid is placed inside a transparent cylinder that is spun about a horizontal axis. A thick mound of liquid forms on the upwardly moving wall. Experiments of Thoroddsen and Mahadevan[18] showed that a pattern of steady periodic fingers often formed, termed ''shark's teeth'' by them. At the rotation speeds and liquid layer thicknesses used in these experiments, both inertial and centrifugal forces were important; thus a direct comparison with the results we will present here is not possible.

In the following section, a mathematical model is developed that will be used for numerical simulation of fingering flows. In addition to the surface tension, gravity drainage, and shear stress contributions to a lubrication-theory evolution equation, we will include an additional term to model finite-contact-angle effects. An analysis involving the interfacial energetics in the neighborhood of an apparent contact line will show that the coefficient of this term is proportional to the square of the static contact angle θ_e for the liquid on the particular substrate material. When the apparent dynamic contact angle is not equal to θ_e, a contribution to the pressure in the liquid arises whose gradients tend to reestablish the equilibrium angle. The model also includes a prescription of a thin, energetically stable, liquid film on nominally dry regions of the substrate. This small thickness plays the role of a slip coefficient and makes moving contact lines possible. The additional pressure is sometimes referred to as ''disjoining pressure'' and has been used in two-dimensional flow simulations by Sharma and Mitlin and co-workers.[20,21] Recently its use has been extended to three-dimensional unsteady simulations by us.[22,23] While not used in the present

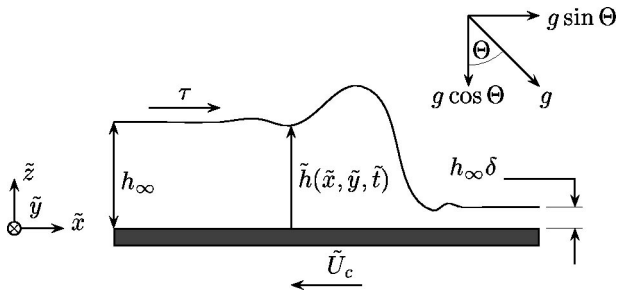

FIG. 2. Definition sketch showing the base state and the coordinate system for the motion of liquid film on an inclined substrate. The coordinates $\tilde{x}$ increases in the flow direction while $\tilde{y}$ is in the transverse direction. $\tilde{z}=\tilde{h}(\tilde{x},\tilde{y},\tilde{t})$ is the surface of the liquid. g is gravity and $\tau=$const is a uniform applied surface shear stress. With a uniform backward translation at a particular speed $\tilde{U}_c$, the base state solution will be independent of time.

paper, the disjoining pressure model can also treat flow on heterogeneous substrates upon which θ_e varies with position.

After nondimensionalization, each problem is shown to possess a one-parameter family of solutions if $\theta_e=0$. The parameter is the wetting-layer thickness δ. For finite θ_e, additional parameter values must be supplied. The present model is compared with another model that allows finite-contact-angle effects. Global or integral norms that can be used to monitor the evolving solution are also introduced.

In Sec. III we discuss the solution technique for the establishment of the two-dimensional base states. By numerically perturbing these solutions, regimes of exponential growth of the integral measures of the disturbances are found. The unsteady algorithm is used to calculate the most unstable growing eigenmodes. For $\theta_e=0$, this early-time behavior is in good agreement with published linear stability calculations.[11,12]

Finger growth in the nonlinear regime is then discussed. For good wetting conditions and a particular realistic value of δ, calculated results are compared directly with the experiments of Cazabat *et al.*[5,13] For gravitational draining, calculated results are presented for both perfect wetting and finite-contact-angle cases. Consistent with experiment, for perfect wetting, solutions evolve to steady-state patterns when viewed in a moving coordinate system. On the other hand, for moderately large values of contact angle, fingers become straight-sided and appear to grow without limit at a constant rate. For even larger values of the contact angle parameter, the fingers do not form these long rivulets. Rather they enter a mode where they periodically shed, or ''pinch off,'' a pattern of droplets.

The concluding section discusses further work, including experiments that could be performed to compare with predictions made here. Incompletely resolved issues, dealing largely with finite contact angle effects, are enumerated.

II. THE MATHEMATICAL MODEL

Figure 2 is a definition sketch for the three-dimensional flow of a thin liquid film on an inclined planar substrate. The coordinate $\tilde{x}$ increases in the flow direction while $\tilde{y}$ measures distance in the transverse direction and $\tilde{z}$ is the elevation perpendicular to the substrate. The substrate is inclined to the horizontal at an angle Θ. The liquid surface is given by $\tilde{z}=\tilde{h}(\tilde{x},\tilde{y},\tilde{t})$ where $\tilde{t}$ is time. An assumed-constant shear stress τ acts on the free surface in the $\tilde{x}$ direction. Such a stress can be produced if the substrate temperature variation is linear and if, in addition, the surface tension is assumed to be a linear function of the temperature.[13] Far upstream the uniform coating thickness is h_∞ while far downstream the thickness is $h_\infty\delta$, where $\delta \ll 1$ is the case of interest. The figure also shows a uniform translation speed $\tilde{U}_c$ in the $-\tilde{x}$ direction. This fictitious speed, found below, is used to render the base-state solutions steady in the moving coordinate system.

The mathematical problem is simplified under the usual assumptions of lubrication theory. We treat an incompressible Newtonian fluid of constant viscosity and assume that inertial forces are negligible, the liquid film is thin, and surface slopes or gradients are small. Defining the areal flux vector as

$$\tilde{\mathbf{Q}}=\int_0^{\tilde{h}}(\tilde{u},\tilde{v})\,d\tilde{z},$$

where $(\tilde{u},\tilde{v})$ are velocity components in the $(\tilde{x},\tilde{y})$ directions, integral mass conservation is

$$\frac{\partial \tilde{h}}{\partial \tilde{t}}=-\tilde{\nabla}\cdot\tilde{\mathbf{Q}}, \tag{2}$$

where the nabla is the two-dimensional gradient operator in $\tilde{x}$ and $\tilde{y}$. The velocity components are found from the creeping-motion momentum equations for almost-parallel flow using the substrate no-slip condition and free-surface normal and tangential stress conditions. Integrating across the film thickness, the flux vector becomes

$$\tilde{\mathbf{Q}}=-\frac{\tilde{h}^3}{3\mu}\tilde{\nabla}\tilde{p}+\left(\frac{\rho g\tilde{h}^3\sin\Theta}{3\mu}+\frac{\tau\tilde{h}^2}{2\mu}-\tilde{U}_c\tilde{h}\right)\mathbf{i}, \tag{3}$$

where $\mathbf{i}$ is a unit vector in the $+\tilde{x}$ direction, μ is viscosity, ρ is density, g is gravitational acceleration, and τ is the constant interfacial shear stress. The pressure $\tilde{p}$ contains a hydrostatic part and a capillary contribution $-\sigma\kappa$ where κ is the surface curvature. Its gradient is

$$\tilde{\nabla}\tilde{p}=-\sigma\tilde{\nabla}\tilde{\nabla}^2\tilde{h}+\frac{\rho g\cos\Theta}{3\mu}\tilde{\nabla}\tilde{h}. \tag{4}$$

The curvature has been replaced by the Laplacian of $\tilde{h}$ which is consistent with the small-slope assumption. These equations can be combined to form a single evolution equation for the coating thickness,

$$\frac{\partial \tilde{h}}{\partial \tilde{t}}=-\frac{\sigma}{3\mu}\tilde{\nabla}\cdot(\tilde{h}^3\tilde{\nabla}\tilde{\nabla}^2\tilde{h})+\frac{\rho g\cos\Theta}{3\mu}\tilde{\nabla}\cdot(\tilde{h}^3\tilde{\nabla}\tilde{h})$$

$$-\frac{\rho g\sin\Theta}{3\mu}\frac{\partial(\tilde{h}^3)}{\partial\tilde{x}}-\frac{\tau}{2\mu}\frac{\partial(\tilde{h}^2)}{\partial\tilde{x}}+\tilde{U}_c\frac{\partial\tilde{h}}{\partial\tilde{x}}. \tag{5}$$

Equation (5) is the leading-order inertialess result that can be derived using the long-wave expansion.[24,25] More recently, the surface shear term has been added to this evolution equation by several authors.[5,7,11]

When suitably nondimensionalized, Eq. (5) can be used to calculate the progression of liquid fronts on fully wetted substrates. The equation is solved over the entire substrate, including areas where the liquid layer is quite thin. While relatively sharp thickness changes, or fronts, occur typically in such problems, it is not necessary to explicitly calculate their positions. The time-dependent frontal motion is captured by the simulation; there is no need to ''fit'' the front locations, since the same physical laws apply to thick and thin regions, as well as to regions where the thickness is rapidly varying. In order to preserve the front-capturing ability of the model for liquid motions on partially wetting substrates that exhibit a finite equilibrium contact angle, we append an additional pressure to the pressure introduced in Eqs. (3) and (4). Termed ''disjoining pressure,'' its gradients are only significant at apparent frontal discontinuities, i.e., in the immediate neighborhood of apparent contact lines.

The disjoining pressure model as introduced by Frumkin[26] and Derjaguin[27] relates observed static contact angles to the intermolecular forces that become important for liquid films of submicroscopic dimensions. The energy density associated with the disjoining pressure $\tilde{\Pi}$ is minimized when the film thickness assumes the very small value $\tilde{h}=\tilde{h}_*$. A simple, computationally convenient, model function is

$$\tilde{\Pi}=B\left[\left(\frac{\tilde{h}_*}{\tilde{h}}\right)^n-\left(\frac{\tilde{h}_*}{\tilde{h}}\right)^m\right], \tag{6}$$

where the exponents n and m are positive constants with $n>m>1$. According to the usual sign convention, the constant B is positive and has the dimensions of pressure. The first term in (6) represents liquid–solid repulsion while the second term is attractive, leading to a stable film thickness at $\tilde{h}=\tilde{h}_*$. $\tilde{\Pi}$ is zero when $\tilde{h}=\tilde{h}_*$ and becomes vanishingly small for $\tilde{h}\gg\tilde{h}_*$.

The energy density associated with (6) is

$$\tilde{e}^{(d)}(\tilde{h})=-\int_{\tilde{h}_*}^{\tilde{h}}\tilde{\Pi}(h')\,dh', \tag{7}$$

which may be observed to have a single stable energy minimum at $\tilde{h}=\tilde{h}_*$. Since the disjoining pressure is assumed to depend on the local interfacial separation $\tilde{h}$ only, with no slope contribution, the validity of expressions (6) and (7) also requires the small free-surface slope approximation.

Consider a macroscopic liquid wedge making an apparent contact angle θ_e with a flat substrate. Apart from the wedge, the substrate is covered with the submicroscopic layer of thickness $\tilde{h}_*$. At equilibrium, the pressure is the total interfacial pressure $\tilde{p}^{\mathrm{I}}=-\sigma\kappa-\tilde{\Pi}$. Note that $\kappa=-d\theta/d\tilde{s}$, where θ is the surface inclination angle relative to the substrate and $\tilde{s}$ is arc length along the liquid surface. Because both contributions to $\tilde{p}^{\mathrm{I}}$ are zero within the uniform thin layer, the net pressure force, on a line perpendicular to the substrate and meeting the wedge surface at an elevation much larger than $\tilde{h}_*$, must also be zero. Thus

$$0=\int_{\tilde{h}_*}^{\infty}\tilde{p}^{\mathrm{I}}(\tilde{h})\,d\tilde{h}=\sigma\int_{\tilde{h}_*}^{\infty}\frac{d\theta}{d\tilde{s}}\,d\tilde{h}-\int_{\tilde{h}_*}^{\infty}\tilde{\Pi}\,d\tilde{h}.$$

But $\sin\theta=-d\tilde{h}/d\tilde{s}$ and this equation integrates to

$$\sigma\cos\theta_e=\sigma-\tilde{e}^{(d)}(\infty).$$

Using (7), the constant B in (6) may be evaluated in terms of the equilibrium contact angle θ_e as

$$B=\frac{(n-1)(m-1)}{\tilde{h}_*(n-m)}\sigma(1-\cos\theta_e)\approx\frac{(n-1)(m-1)}{2\tilde{h}_*(n-m)}\sigma\theta_e^2, \tag{8}$$

and the small argument approximation to $\cos\theta_e$ is used for the approximate equality. A more complete derivation of (8) as well as plots of disjoining pressure and disjoining energy density for several different exponent pairs (n,m) may be found elsewhere.[22]

Disjoining pressure is, in the present model, an additional interfacial effect that may be thought of as a modification to the capillary pressure. Like capillary pressure, its value at any location depends only on the shape of the liquid film. Gradients of $\tilde{\Pi}$ drive liquid motion but the effect is only important in the immediate vicinity of apparent contact lines. For cases treated here, θ_e^2, which controls the magnitude of this additional pressure gradient, is taken constant over the entire substrate. Thus for contact line motion on partially wetting substrates the evolution equation (5) becomes

$$\begin{aligned}\frac{\partial\tilde{h}}{\partial\tilde{t}}=&-\frac{\sigma}{3\mu}\tilde{\nabla}\cdot(\tilde{h}^3\tilde{\nabla}\tilde{\nabla}^2\tilde{h})+\frac{\rho g\cos\Theta}{3\mu}\tilde{\nabla}\cdot(\tilde{h}^3\tilde{\nabla}\tilde{h})\\&-\frac{\rho g\sin\Theta}{3\mu}\frac{\partial(\tilde{h}^3)}{\partial\tilde{x}}-\frac{\tau}{2\mu}\frac{\partial(\tilde{h}^2)}{\partial\tilde{x}}+\tilde{U}_c\frac{\partial\tilde{h}}{\partial\tilde{x}}\\&-\frac{\sigma}{3\mu}\frac{(n-1)(m-1)\theta_e^2}{2\tilde{h}_*(n-m)}\tilde{\nabla}\cdot\left(\tilde{h}^3\tilde{\nabla}\left[\left(\frac{\tilde{h}_*}{\tilde{h}}\right)^n-\left(\frac{\tilde{h}_*}{\tilde{h}}\right)^m\right]\right).\end{aligned} \tag{9}$$

This additional term allows the interfacial energetics to influence the motion in a number of ways. Because a particular finite contact angle is energetically favored, spontaneous motions, not driven by applied body or surface forces, will tend to establish or reestablish this angle where a thick liquid region meets the substrate. For forced motion, *onto* a sensibly dry substrate, as for the two-dimensional motions shown schematically in Fig. 1, the advancing contact angle will be determined principally by the magnitude of the driving force, if this force is large; then the equilibrium angle may cause only a small change in the dynamic angle. Dewetting motions, where the liquid recedes from the substrate, can also exhibit a finite dynamic angle because of this term. It is also possible, without significant additional difficulty, to model motions on heterogeneous substrates where θ_e is a

given function of position. Calculations for three-dimensional unsteady droplet motions in both spontaneous and forced cases have recently appeared.[22,23] Experimental comparison, for a particular wettability pattern, shows detailed qualitative agreement[23] but the predicted motion is too rapid, by an order-one factor, for reasons explained later. Other studies have reported two-dimensional simulation results using various forms of disjoining pressure.[20,21,28–30]

There are significant differences in the interpretation of the mathematical model, depending on whether θ_e is negligibly small or finite. For motions on prewetted substrates when the contact angle is very small, disjoining pressure effects are negligible. The preexisting downstream wetting layer thickness $h_\infty\delta$ may take on any value. For partially wetting systems, on the other hand, disjoining effects are important. Physically reasonable values of $\tilde{h}_*$ are very small and can be expected to be measured in nanometers. It is possible to estimate $\tilde{h}_*$ for particular systems using physicochemical principles.[26,27] Because contact line motion to or from perfectly dry substrate areas is impossible without some form of relaxation of the no-slip condition,[9] it is clear that $\tilde{h}_*$ is a type of slip coefficient. When the present model is used, dynamic experimental studies can provide an independent determination or verification of $\tilde{h}_*$. By considering the viscous dissipation at the ''foot'' of a moving liquid front, the dependence of the speed on $\tilde{h}_*$ can be estimated. A given driving force per unit contact-line length F will produce motion at a speed U given by the relation

$$F = \text{const}\,\frac{\mu U}{\theta_e}\log\left(\frac{\tilde{h}_1}{\tilde{h}_*}\right),$$

where $\tilde{h}_1$ is some macroscopic reference film thickness.[31] This dependence on $\tilde{h}_*$ is remarkably weak; thus a value of $\tilde{h}_*$ that is overly large by a factor of 10^3 can be expected to produce motions that are too rapid by a factor between 2 and 3. Numerical limitations in the present three-dimensional simulations require us to use $\tilde{h}_*$ that are too big by a similar factor. Thus spontaneous aspects of calculated motions can be expected to be too rapid by the order-one factors. In the following we will replace $\tilde{h}_*$ by $h_\infty\delta$; that is, for partially wetting systems, the preexisting layer thickness will be taken to be the energetically stable value.

It is useful to comment on the dynamical role of the exponents in the disjoining pressure expression (6). The disjoining model used here has a single stable energy minimum at $\tilde{h}=\tilde{h}_*$ and the term is only important when $\tilde{h}$ is close to this value. For slow motion of apparent contact lines, the contact angle will change from its equilibrium value in response to this motion. The magnitude of this deviation is controlled by the local shape of the energy ''well'' at $\tilde{h}=\tilde{h}_*$ as given by the curvature

$$\left[\frac{\mathrm{d}^2\tilde{e}^{(d)}}{\mathrm{d}\tilde{h}^2}\right]_{\tilde{h}=\tilde{h}_*} = -\left[\frac{\mathrm{d}\tilde{\Pi}}{\mathrm{d}\tilde{h}}\right]_{\tilde{h}=\tilde{h}_*} = \frac{\sigma\theta_e^2}{2\tilde{h}_*^2}(m-1)(n-1)$$

using (6) and (8). The choice of exponent pairs (n,m) determines the steepness of the energy well. Current theory, as summarized by Teletzke *et al.*,[32] indicates that disjoining pressure contributions, while not completely understood, are strongly dependent on the particular liquid–solid material system and may include molecular (Van der Waal's), ionic-electrostatic, and so-called structural contributions. A relatively simple functional such as (6) can only approximate these various combined effects.

Most of the calculations presented here use the exponent pair (3,2). Several simulations have been repeated using the pair (4,3) which has a steeper energy well. Consistent with previous computational work[22,23] we find that the evolution of the fingering pattern is determined primarily by the value of the equilibrium angle θ_e, rather than the choice of (n,m). The relatively minor dynamical effect of the exponent choice is demonstrated in Sec. III B.

Here we treat only two special cases of the evolution equation (5). These motions are vertically draining films due to gravity, and vertically ascending films caused by application of a constant surface shear stress. Both perfect wetting and finite-contact-angle cases will be considered for each of these.

A. Gravity-driven draining films

Consider downward draining on a vertical substrate ($\Theta=\pi/2$), without surface shear stress. Far upstream the fluid layer is uniform with a thickness h_∞, while far downstream the thickness is $h_\infty\delta$. A steadily propagating solution can be shown to move at a speed $\tilde{U}_e$ given by

$$\tilde{U}_c = \frac{\rho g h_\infty^2}{3\mu}(1+\delta+\delta^2),$$

which is seen to be virtually independent of δ for $\delta \ll 1$. This expression is readily obtained by noting that, for a steadily moving waveform, the flux must be constant in the wave-fixed system and that neither surface tension nor disjoining pressure gradients contribute to the flux when the layer is flat.[10] For convenience we will move the substrate at this speed so the two-dimensional base state is stationary.

We introduce dimensionless variables by

$$x=\frac{\tilde{x}}{L},\quad y=\frac{\tilde{y}}{L},\quad h=\frac{\tilde{h}}{h_\infty},\quad \text{and}\quad t=\tilde{t}\frac{\sigma h_\infty^3}{3\mu L^4}, \tag{10}$$

where L is a characteristic substrate length given by

$$L = h_\infty(3\,\mathrm{Ca})^{-1/3}.$$

$\mathrm{Ca}=\mu U/\sigma$ is a capillary number based on the average upstream flow speed U. This choice of characteristic quantities makes the coefficients of both the surface tension and driving force terms equal to unity. The introduction of Ca allows the gravity-driven film and the surface-traction-driven film to use the same nondimensionalization. For gravity-driven flow

$$\mathrm{Ca}=\frac{\rho g h_\infty^2}{3\sigma}.$$

Using the new variables, the dimensionless evolution equation is

$$\frac{\partial h}{\partial t}=-\nabla\cdot(h^3\nabla\nabla^2 h)-\frac{\partial(h^3)}{\partial x}+(1+\delta+\delta^2)\frac{\partial h}{\partial x}$$
$$-K\nabla\cdot\left(h^3\nabla\left[\left(\frac{\delta}{h}\right)^n-\left(\frac{\delta}{h}\right)^m\right]\right), \tag{11}$$

where the dimensionless contact angle parameter is

$$K=(3\,\mathrm{Ca})^{-2/3}\frac{(n-1)(m-1)\theta_e^2}{2\delta(n-m)}. \tag{12}$$

B. Surface-shear-stress-driven ascending films

For sufficiently thin films, $\tilde{h}\ll\tau/(\rho g)$ and the backward gravitational drainage is negligible compared to the flow produced by a constant surface shear stress. This condition is satisfied in the experiments of Cazabat *et al.*,[5,13] using (1), for sufficiently *small* values of τ, specifically when the characteristic length σ/τ is much greater than the capillary length $\sqrt{\sigma/\rho g}$. For an ascending film $\Theta=-\pi/2$. Again, assuming flat films both upstream and downstream, the speed of frontal motion for this problem can be shown to be[11]

$$\tilde{U}_c=\frac{\tau h_\infty}{2\mu}(1+\delta).$$

Using the nondimensionalization (10) the evolution equation becomes

$$\frac{\partial h}{\partial t}=-\nabla\cdot(h^3\nabla\nabla^2 h)-\frac{\partial(h^2)}{\partial x}+(1+\delta)\frac{\partial h}{\partial x}$$
$$-K\nabla\cdot\left(h^3\nabla\left[\left(\frac{\delta}{h}\right)^n-\left(\frac{\delta}{h}\right)^m\right]\right), \tag{13}$$

with K given by (12) and

$$\mathrm{Ca}=\frac{\tau h_\infty}{2\sigma}.$$

Note that, apart from the arbitrarily imposed translational speeds, the two problems differ only through the driving terms: $\partial(h^3)/\partial x$ in (11) versus $\partial(h^2)/\partial x$ in (13).

C. Two-dimensional steady-state solutions

We calculate the base-state solutions for the two flows shown in Fig. 1. For gravity-driven draining films, in a wave-fixed coordinate system, the dimensionless areal flux at any x station is $-(\delta+\delta^2)$. We include disjoining effect and choose the exponent pair $(n,m)=(3,2)$. The resulting ordinary differential equation is

$$h_{xxx}=-1+\frac{1+\delta+\delta^2}{h^2}-\frac{\delta+\delta^2}{h^3}-\frac{K\delta^2}{h^3}\left(2-\frac{3\delta}{h}\right)h_x, \tag{14}$$

where subscripts denote differentiation. Because x does not explicitly appear, the equation is translationally invariant and requires only the two boundary conditions

$$h(x\to-\infty)\to 1,\quad h(x\to+\infty)\to\delta.$$

The equation is solved numerically by a shooting method. Initial conditions are generated from a simplified version of the equation valid far upstream where the uniform layer is only slightly perturbed. Let $h\approx 1+\eta$ and assume $|\eta|\ll 1$. Here η satisfies the linear equation

$$\eta_{xxx}+K\delta^2(2-3\delta)\eta_x+(2-\delta-\delta^2)\eta=0 \tag{15}$$

with solutions of the form $\eta\sim e^{qx}$ where q satisfies a cubic equation. Provided

$$\frac{K^3\delta^6}{27}(2-3\delta)^3+\left(-1+\frac{\delta}{2}+\frac{\delta^2}{2}\right)^2>0,$$

there is one negative real root and a pair of complex conjugate roots with positive real part. This inequality holds for all $K>0$, for $\delta<\frac{2}{3}$. The real root produces a component that decays as x increases. Therefore initial values of h, h_x, and h_{xx} are generated from the upstream limiting solution

$$h\to 1+a\,e^{bx}\cos(cx),$$

where a is an arbitrary but small parameter, and b and c are the real and imaginary parts of a complex root, phase being unimportant. a is taken small, on the order of 10^{-6} or smaller, and is varied until the downstream condition is satisfied to high accuracy. Here a must be chosen from a discrete sequence of small values where the ratio of any two successive members of the sequence is a particular number that depends on K. This ratio is about 37.62 when K is zero.[10] Numerical integration of (14) is performed using a fourth-order Runge-Kutta solver.

The corresponding differential equation for the stress-driven ascending film is

$$h_{xxx}=-\frac{(h-1)(h-\delta)}{h^3}-\frac{K\delta^2}{h^3}\left(2-\frac{3\delta}{h}\right)h_x, \tag{16}$$

and is solved similarly. Each problem has a two-parameter (K,δ) family of solutions. For $K=0$, solutions obtained by the shooting method are available for each problem.[10,11] In general, as δ is reduced, both the maximum overshoot and the maximum profile slope (an apparent advancing contact angle) increase. Each of these tend to infinity as $\delta\to 0$ reflecting the impossibility of moving a contact line onto a perfectly dry substrate.

Figure 3 show profiles for various K, for a particular value of δ, for each of the two problems. For the range of K values shown, there is monotonic increase in the overshoot with increasing K and a small increase in the maximum profile slope. The frontal height and undulation wavelength are seen to be greater for the stress-driven case.

The role played by disjoining pressure in the present model can be further clarified by examining, in more detail, the changes in the maximum slope caused by finite K values. Consider the gravity problem with $0<K\ll 1$. The solution to (14) is expanded as

$$h(x)=h_0(x)+Kh_1(x)+O(K^2). \tag{17}$$

Here $h_0(x)$ will satisfy (14) with $K=0$ while $h_1(x)$ is the solution of

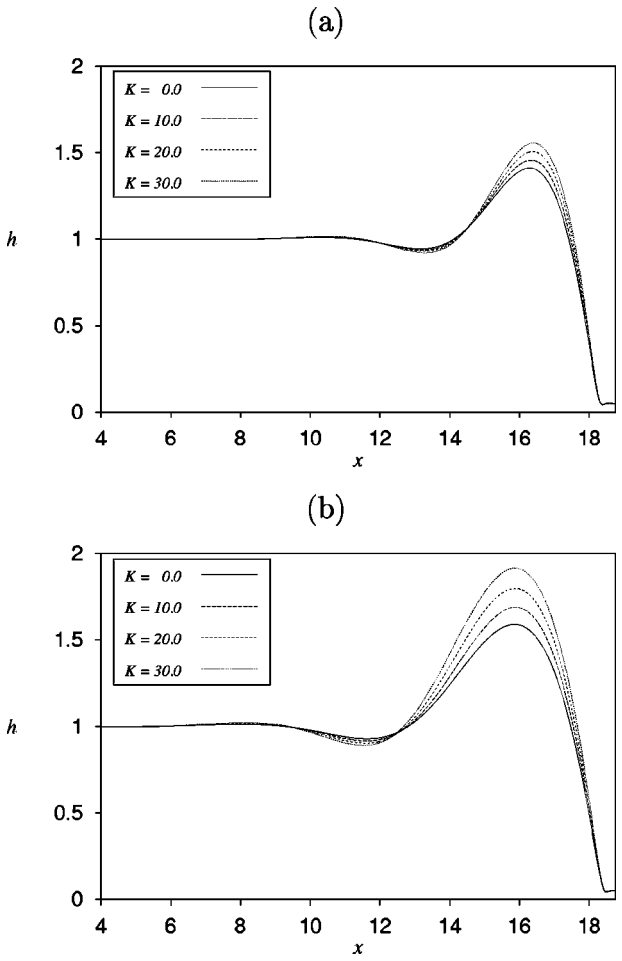

FIG. 3. Two-dimensional base-state thickness profiles for (a) gravity-driven flow, as calculated from (14), and (b) surface-shear-stress-driven flow using (16). The prewetted layer thickness is $\delta=0.05$. Results are shown for various values of the equilibrium contact angle parameter K for each problem.

$$h_{1xxx}=-\left(2\frac{1+\delta+\delta^2}{h_0^3}-3\frac{\delta+\delta^2}{h_0^4}\right)h_1 - \frac{\delta^2}{h_0^3}\left(2-\frac{3\delta}{h_0}\right)h_{0x}, \tag{18}$$

subject to the homogeneous boundary conditions $h_1(\pm\infty)=0$. This linear differential equation is forced by the calculated function $h_0(x)$. It is convenient to solve equations (14) and (18) simultaneously by the Runge–Kutta shooting method. Let x_1 be the value of x at which $|h_{0x}|$ is a maximum. Then the maximum slope, by Taylor series expansion for finite K from (17), is

$$h_x(x^*)=h_{0x}(x_1)+Kh_{1x}(x_1)+O(K^2). \tag{19}$$

The maximum slope will occur at another value $x=x^*\neq x_1$ and it may be shown that x^*-x_1 is also $O(K)$.

Within the present small-slope analysis, the maximum slope, as predicted by (19), may be identified with the dynamic contact angle θ_d. Moreover, from (12), $K\delta\sim\theta_e^2$. Thus (19) may be rewritten, in scaled form, as

$$\theta_d=(3\mathrm{Ca})^{1/3}\left[a+b\left(\frac{\theta_e}{(3\mathrm{Ca})^{1/3}}\right)^2\right], \tag{20}$$

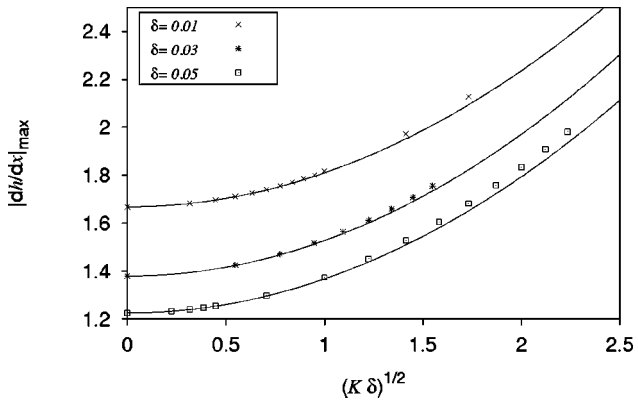

FIG. 4. Apparent dynamic contact angle θ_d versus static contact angle θ_e for the base-state of the gravity-driven flow problem using scaled variables. $|dh/dx|_{\max}\approx\theta_d(3Ca)^{-1/3}$, and $(K\delta)^{1/2}\approx\theta_e(3\mathrm{Ca})^{-1/3}$. Solid lines are approximate solutions, valid for small θ_e, using Eq. (20).

where the functions $a(\delta)$ and $b(\delta)$ are determined numerically. Figure 4 compares the small-K prediction of (20) with shooting-method solutions of (14) for three values of δ. The predicted parabolic dependence is seen to be satisfactory provided K is not overly large. In the large-K limit, each curve will asymptote to $\theta_d\approx\theta_e$ as the interfacial effects will then dominate dynamic forces.

It is interesting to note that the structure of the solution family in Fig. 4 is quite equivalent to the predicted dependence of θ_d on θ_e that would arise from an entirely different method for treating contact line motion. In the treatment of the steady two-dimensional gravity drainage problem given by Tuck and Schwartz,[10] the slip model due to Greenspan is also considered.[33] In that model the equation that replaces (14) is

$$h_{xxx}=-1+\frac{1+\alpha}{h^2+\alpha}. \tag{21}$$

The model (21) allows contact line motion by removing the singularity at $h=0$. The slip coefficient α is a small positive number. Using the Greenspan model, it is possible to integrate the profile until it meets the substrate at a finite contact angle. This angle may be identified with θ_e, while the maximum slope, or θ_d, will depend on θ_e and α. Figure 10 of that paper[10] shows calculated curves of θ_d versus θ_e for several different small values of the slip parameter α. That figure is structurally identical to Fig. 4; in both theories the dynamic angle increases as the small parameter, α in (21) versus δ in (14), is reduced. Both exhibit parabolic behavior for small θ_e and linear dependence when θ_e becomes relatively large. By performing a set of calculations, it would be possible to find a function, $\delta(\alpha)$ say, that would yield similar profiles (for this particular problem). This is consistent with the interpretation of δ as a slip coefficient. Recently an adaptation of the Greenspan model has been used to simulate nonlinear rivulet dynamics[34]. It would not appear to be possible, however, to employ the Greenspan model in three-dimensional dynamic simulations without explicit tracking of contact lines and imposition of the static contact angle at

each time instant at all points along the lines. Nor does the Greenspan model (21) have an immediate interpretation in terms of interfacial energetics.

D. Integral measures of disturbance growth

It is useful to define one or more functions of time to characterize the state of the growing finger pattern. Such a space-integrated measure will serve two distinct purposes. For the early stages of growth, it will allow direct comparison with the available linear stability analyses of the gravity-driven and shear-driven problems.[11,12] At later times it will be used as an indicator of the ultimate pattern, specifically whether it becomes (i) steady, in a moving reference frame, (ii) unsteady with fingers growing at a constant speed, or (iii) unsteady and time periodic.

One measure is the capillary energy of the liquid surface. This is equal simply to the surface area times the surface energy density or surface tension σ. We look at the difference between this energy and the energy of a perfectly flat surface which is

$$\sigma \int \int \left(\frac{1}{\cos \gamma} - 1 \right) d\tilde{A} \approx \frac{\sigma}{2} \int \int \tilde{\nabla} \tilde{h} \cdot \tilde{\nabla} \tilde{h} \, d\tilde{A}, \tag{22}$$

where γ is the angle between the free-surface and substrate normal vectors and $\tilde{A}$ is the total area of the substrate. The approximate equality follows from use of the small-slope approximation. In dimensionless terms, the latter is

$$E^{(\sigma)} \equiv \frac{1}{2} \int \int \nabla h \cdot \nabla h \, dA, \tag{23}$$

where $E^{(\sigma)}$ is measured in units of (σh_∞^2). The area element $dA = dx\, dy$ and, for definiteness, we take the width of the domain to be one-half of a wavelength in the y or transverse direction. For the problems considered here, the liquid surface becomes flat as $x \to \pm\infty$. Thus the calculated energy using (23) is a unique function of time provided the x domain extends sufficiently far upstream and downstream of the front and finger region.

The early time growth rate of small perturbations to the base-state solution may be found by monitoring $E^{(\sigma)}(t)$. Define h_0 to be the base state in the moving coordinate system and let

$$h(x,y,t) = h_0(x) + h_1(x,y,t), \tag{24}$$

where $|h_1| \ll |h_0|$. It is sufficient to assume that

$$h_1(x,y,t) = g(x) \cos(ky) \exp(\beta t), \tag{25}$$

where $g(x)$ is a disturbance eigenfunction to be determined, $k = 2\pi/\lambda$ is the transverse wave number of a disturbance, and $\beta(k)$ is the growth rate of the perturbation. The surface energy integral is then

$$E^{(\sigma)} = \frac{1}{2} \int dx \int_0^{\pi/k} dy \times \left[\left(\frac{dh_0}{dx} \right)^2 + 2 \frac{dh_0}{dx} \frac{\partial h_1}{\partial x} + \left(\frac{\partial h_1}{\partial x} \right)^2 + \left(\frac{\partial h_1}{\partial y} \right)^2 \right]. \tag{26}$$

The y integrations can be performed explicitly, yielding

$$E^{(\sigma)} - E_0^{(\sigma)} = \frac{\pi}{8k} \exp(2\beta t) \int \left[\left(\frac{dg}{dx} \right)^2 + k^2 g^2 \right] dx, \tag{27}$$

where

$$E_0^{(\sigma)} = \frac{\pi}{2k} \int \left(\frac{dh_0}{dx} \right)^2 dx.$$

The numerical solution of either evolution, (11) or (13), will be initiated with a small sinusoidal perturbation to the base state. Provided the perturbation is quite small, its specific form, in x, is irrelevant. Because each equation is nonlinear, any perturbation will quickly ''seed'' all possible disturbance modes. For any given k, exponential growth of the capillary energy for the most unstable mode $g(x)$ will be observed. This will persist over several decades in amplitude, provided the growing perturbation is still small in absolute terms. In view of (27), a plot of $\log(E^{(\sigma)} - E_0^{(\sigma)})$ versus time will have slope 2β. By running a number of short computations with different values of k, the wavelength for which β is largest can be identified. The corresponding eigenfunction of maximum growth $g(x)$ can then be extracted using (24) and (25). This procedure is equivalent to the more traditional stability analyses that find the numerical solution of the discrete eigenvalue problem associated with the linearized form of the evolution equation appropriate to small perturbations[11,12]. Comparison with the linear stability results is a useful check for the nonlinear algorithm.

An alternative norm, which also can serve to characterize the finger pattern, is[12]

$$\|h_1\| \equiv \frac{1}{2} \int \int (h_1)^2 \, dA. \tag{28}$$

When g is small, it is simply given by

$$\|h_1\| = \frac{\pi}{8k} \exp(2\beta t) \int g^2 \, dx \tag{29}$$

and may thus be used in the same manner as (27) to identify appropriate values of k, β, and the function g. Unlike the capillary energy norm that can be calculated in a coordinate system that translates at any speed, the norm (29) requires that the subtraction $h - h_0$ be performed for a profile that moves at the speed of the base state.

III. IMPLEMENTATION AND RESULTS

A. Numerical techniques and computational issues

Equation (11) or (13) is solved using time-marching finite-difference methods. Straightforward explicit time-marching requires that time steps be very small in order to maintain numerical stability; specifically Δt must be no larger than order Δ^4, where Δ is the space step or mesh size. Thus the computational requirement quickly becomes more severe as the mesh size becomes small for an explicit method. We have found that Δ must be somewhat smaller than the wetting-layer thickness δ, in dimensionless units, in order to maintain accuracy in the ''contact region'' where fronts or finger edges meet the wetting layer.

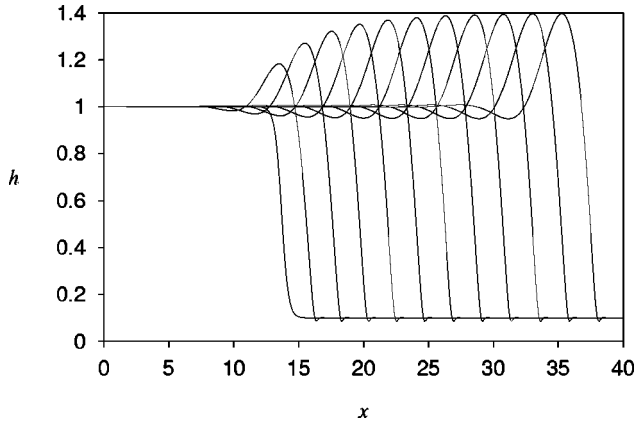

FIG. 5. The development in time of the two-dimensional steady-state profile starting from an arbitrary initial configuration for stress-driven flow. The dimensionless time interval between profiles is $\Delta t \approx 2.0$. The grid spacing is $\Delta = 0.006$. Other parameter values are $\delta = 0.1$ and $K = 0$.

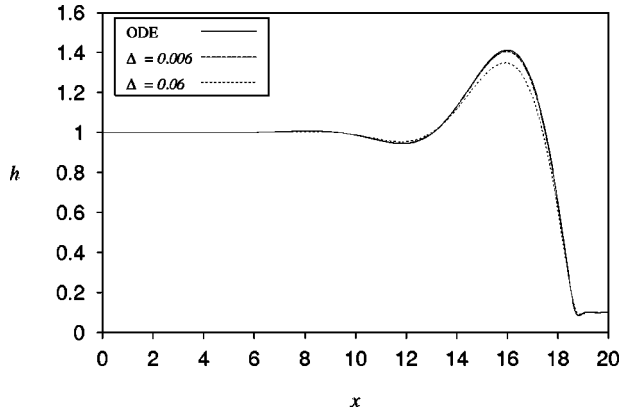

FIG. 6. Steady-state profiles for stress-driven flow. Solution of the ordinary differential equation (16) is compared with the long-time results of unsteady calculations using two different mesh sizes Δ. Here $K = 0$, $\delta = 0.1$.

In order to overcome the time step size limitation, the quasi-three-dimensional solutions given here use an alternating-direction-implicit (ADI) technique.[35–37] The ADI technique uses alternating sweeps in each direction and a banded system of equations is solved to update the discrete set of $h_{i,j}$ values in a row or column. Maximum permissible time steps can be as much as a factor of 10^5 larger than the characteristic maximum step for stability for an explicit method. Apparent contact lines are captured by the method and their motion appears as part of the evolving solution. Nonlinear prefactors in the equations are evaluated at the previous time level.

It has been found that an adaptive time-stepping procedure, where the time step is adjusted dynamically based on a preset maximum permissible change in any h value, greatly increases computational efficiency. Motions with strong capillary effect often exhibit alternating slow and rapid events as the liquid pattern evolves. Thus a time integration scheme that is able to adapt to these changes is particularly appropriate. Temporal convergence is verified by reducing the allowed maximum change in h. Further details of the basic numerical methods employed here may be found elsewhere.[23,38,39]

Graphical output of evolving profile shapes can be stored and the results later displayed sequentially as a ''movie.'' Run times varied from a few minutes when the computational ''window'' is small to more than 24 h when long fingers are calculated. Computational times are proportional to the number of unknowns; thus the penalty for using larger domains is modest relative to methods that require full matrix inversions. Unless otherwise stated, profiles are calculated in a coordinate system that is moving at the constant frontal speed of the two-dimensional base state.

As an introductory example, we show results of a two-dimensional unsteady calculation in Fig. 5. The starting profile is an arbitrarily selected hyperbolic-tangent function that joins the upstream and downstream constant-thickness layers. For this stress-driven flow, profiles are moving relative to a fixed substrate. As can be observed, about 20 time units are required for steady-state conditions to be achieved. In steady propagation the profile moves at a dimensionless speed $1+\delta$ as given by Eqs. (13).

Figure 6 compares the steady-state profile shape for this case with the effectively exact results of the shooting-method solution of the ordinary differential equation (16). For a mesh size $\Delta = 0.006$, the profiles are seen to be graphically indistinguishable. Also shown is the result of an unsteady calculation using the coarser mesh $\Delta = 0.06$. This coarser mesh is representative of those used in the three-dimensional cases to be presented later. It may be observed that the maximum crest height, for example, is 4.5% less than the exact value.

B. Three-dimensional calculations

Figures 7–10 show early-time results of the simulation for both the stress- and gravity-driven problems. A principal purpose of these computations is comparison with published linear stability analyses.[11,12] The base state solutions in the simulation were perturbed with a small $O(10^{-8})$ sinusoidal ''wiggle'' in the neighborhood of the crest. The exact form and location of this starting ''seed'' was demonstrated to be unimportant, as expected. Figure 7 contains plots of the integral norm (28) versus time for several transverse ''window'' widths or wave numbers k. Linear behavior on these semilogarithmic graphs indicates exponential growth of the disturbance norm. In this regime, which can be seen to persist over a number of decades, a linearized form of the evolution equation is also valid, allowing direct comparison with the linear results. For each problem, three curves are shown, corresponding to the wave number of maximum growth and wave numbers that are somewhat larger and smaller. The slope of each graph yields the growth rate β.

Figure 8 shows the dependence of the calculated growth rate function $\beta(k)$ on the mesh size used in the calculations. The solid curves were compiled from results similar to those shown in Fig. 7. As the mesh size is reduced, both the critical wave number and maximum growth tend towards the values read from the graph of Spaid and Homsy[12] for this value of precursor thickness δ. Their result was found by linearizing the evolution equation and solving the resulting fourth-order eigenvalue problem numerically for the eigenfunction $g(x)$.

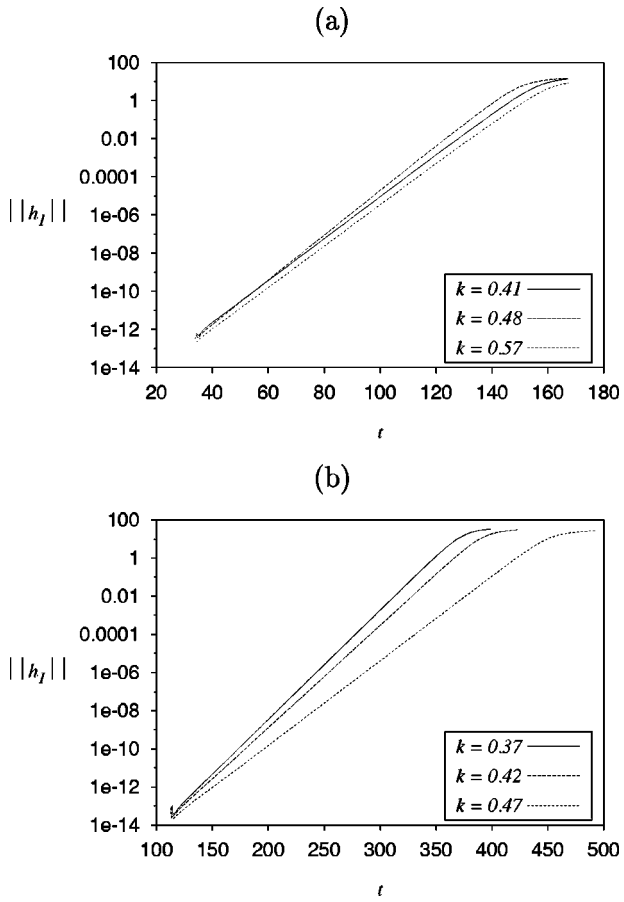

FIG. 7. Temporal evolution of an integral norm, defined in (28), that is used to measure the deviation of the evolving profile from the base state after imposition of a small perturbation. A straight line indicates exponential growth. Several different wave numbers k are compared in order to identify the fastest growing mode; (a) gravity-driven and (b) stress-driven flow problems. Here $\delta=0.05$, $K=0$.

Had a mesh size equal to the (unreported) size used in the linear stability calculations been used, it is likely that very similar results would have been obtained. For the fine mesh $\Delta=0.0225$, the most unstable wave number is $k_m\approx 0.48$ in

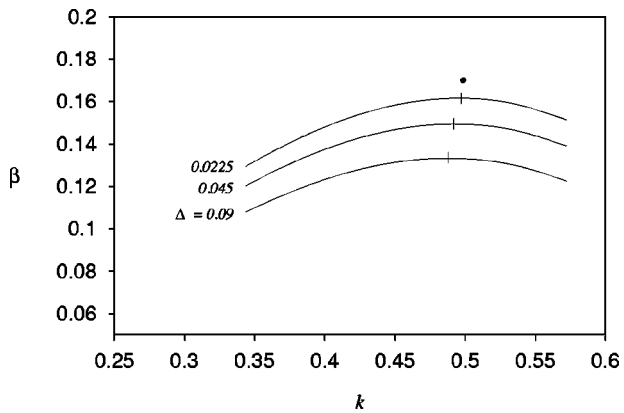

FIG. 8. The effect of mesh size Δ on the initial growth rate β for gravity-driven flow; $K=0$, $\delta=0.05$. Solid lines are spline fits to growth rate values obtained by nonlinear simulation. Tic marks indicate maxima. The dot is the maximum growth rate from the solution of the eigenvalue problem (Ref. 12).

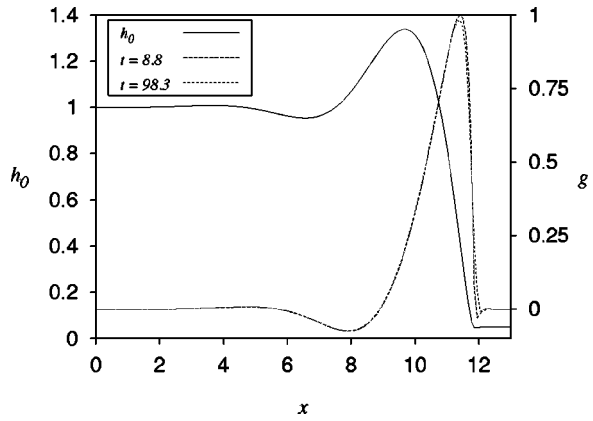

FIG. 9. The normalized eigenmode $g(x)$ for the most unstable wave number superposed on the base-state profile $h_0(x)$. Gravity flow. Eigenmodes at two different times, in the linear regime, are virtually indistinguishable; $K=0$, $\delta=0.05$.

good agreement with their value. For the stress-driven flow, the most unstable wave number, calculated in the same way, is $k_m\approx 0.36$ for $K=0$ and $\delta=0.05$. This value is close to that reported by Kataoka and Troian,[11] who also solved an eigenvalue problem to find the dispersion relationship.

The eigenfunction corresponding to the wave number of maximum growth is shown in Fig. 9. It is calculated from the numerical functions $h(x,y,t)$ and $h_0(x)$ according to

$$g(x)=\frac{2k}{\pi e^{\beta t}}\int_0^{\pi/k}(h-h_0)\cos ky\ \mathrm{d}y. \tag{30}$$

Results at two times, both within the linear regime, are shown superimposed on the base state in the figure. The eigenmode is essentially invariant, as expected, and agrees well with the one calculated by Spaid and Homsy.[12] Note that its peak is approximately centered on the forward face of the capillary ridge of the base state.

A similar calculation of growth rate versus wave number, to illustrate the effect of finite contact angle, is shown in Fig. 10 for the stress-driven problem. For $K>0$, the wavelength of maximum growth decreases somewhat. A more

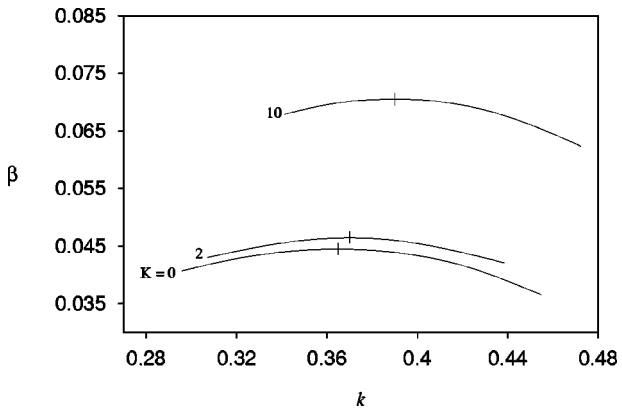

FIG. 10. Early-time growth rate β versus wave number k for stress-driven flow; perfectly wetting and finite-contact-angle cases are compared. As the contact angle θ_e increases, both the growth rate and maximum-growth wave number increase. The parameter K is proportional to θ_e^2. Here $\delta=0.1$, $\Delta=0.05$.

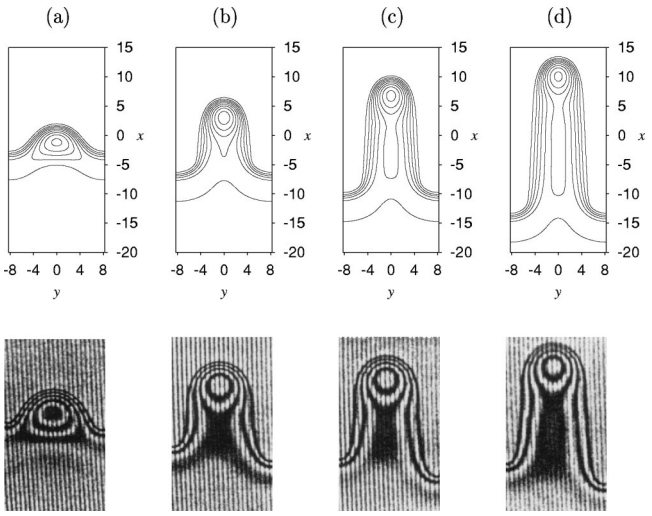

FIG. 11. Comparison of theoretical results with experiment for Marangoni-stress-driven flow on a vertical plate. Physical parameters and interferometric photographs are taken from Cazabat *et al.* (Ref. 5) (with permission from Elsevier Science Publishers.) See text for physical parameter values in the experiment. Using these values, the predicted finger width is 0.42 mm compared with a measured average value of 0.44 mm. The interval between the pictures for the computation is 5.7 mins. The experimental pictures were not taken at equal time intervals; the average of the time intervals was about 5 min. (Ref. 13) The dimensionless thickness difference between contours is $\Delta h = 0.25$. Two contours correspond to one full fringe in the interferographs.

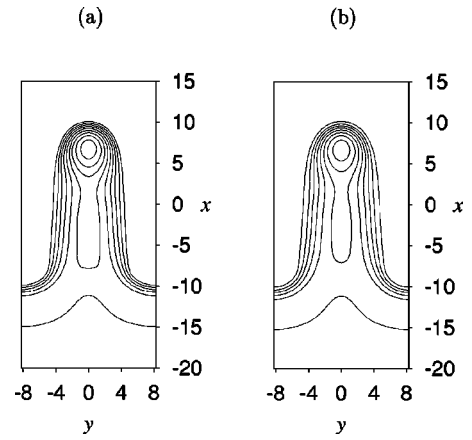

FIG. 12. The effect of wetting layer thickness δ on the finger shape for Marangoni-stress-driven flow, $t = 460$. (a) $\delta = 0.025$; (b) $\delta = 0.05$. $\delta = 0.05$, as used in Fig. 11, provides a better fit to the experiment. The thickness difference between contours is $\Delta h = 0.25$.

pronounced effect is a large increase in growth rate β. This is, no doubt, associated with the increase in the height and curvature of the capillary ridge as K increases, as shown in Fig. 3.

Figure 11 shows a comparison between computed results and the Marangoni-stress-driven experiments of Cazabat *et al.*[5] Reported experimental values are $\sigma = 20\,\mathrm{mN/m} = 20\,\mathrm{dyn/cm}$, $\mu = 20\,\mathrm{mPas} = 0.2\,\mathrm{P}$ and an upstream thickness $h_\infty = 0.45\,\mu\mathrm{m}$. This thickness is almost exactly equal to the total height difference for two interference fringes using the given values of laser light wavelength and index of refraction. There is some uncertainty in the τ value since the pictures presented do not correspond precisely to any particular tabulated case.[5] However, in a companion paper,[13] the value $\tau = 0.18\,\mathrm{N/m^2} = 1.8\,\mathrm{dyn/cm^2}$ is reported. The average spacing between fingers was $\lambda_{\mathrm{exp}} = 0.44\,\mathrm{mm}$, interpolated from tabular values. A precursor layer, if present, would be far too thin to be detectable with interferometry and no such value was reported. The time intervals between the experimental frames was not constant but an average value was about 5 min.[13] Each experimental picture in Fig. 11 was cropped from a group of three shown in the original paper.

The simulation results in the figure used a dimensionless precursor thickness $\delta = 0.05$ or 22.0 nm in physical units. Using the given values of h_∞, σ, and τ, the substrate reference length is $L = 0.002\,45\,\mathrm{cm}$. The wavelength of maximum growth is then $\lambda_{\mathrm{calc}} \approx 17L \approx 0.42\,\mathrm{mm}$, only slightly smaller than λ_{exp}. The spacing between contour lines for the simulation is $0.25\,h_\infty$ so that two contour lines correspond to one fringe in the experiment. The characteristic time for the simulation is $T^* = 3\mu L^4/(\sigma h_\infty^3) \approx 11.9\,\mathrm{sec}$. Thus the elapsed time between calculated frames, 29 dimensionless units, becomes 5.7 mins. The simulation frames are shown in a coordinate system translating at the base-state speed. The equivalent position of the base state corresponds to the $x = 0$ mark in each figure. The simulation results are seen to be in substantial agreement with the experimental pictures, including the appearance of a secondary height maximum that develops behind the bulbous leading edge of the growing finger.

The precursor thickness δ was selected so as to match the height maximum of the bulbous finger tip. In Fig. 12, the contour map using the last picture in Fig. 11 is compared with the contour map when $\delta = 0.025$. Little difference is seen; thus $\delta = 0.025$ is also considered to be a plausible choice. Reducing δ is seen to make the central height slightly larger and also to reduce the finger width a small amount.

While the agreement between λ_{calc} and λ_{exp} is remarkably good and the time scale for finger growth also matches the experiment, it should be noted that the theoretical prediction of h_∞ in Eq. (1) is high by about a factor of 2 compared to the measured value. The theory leading to (1) does not consider backward gravity drainage. Although the predicted value would be reduced somewhat if this effect were to be included, the correction is expected to be small. A more likely explanation for the discrepancy is nonconstancy of the temperature gradient and resulting variation in the applied shear stress.

For motions on a prewetted substrate of sufficient surface energy that finite-contact-angle effects are negligible, finger profiles will eventually achieve a steady-state configuration. This is illustrated in Fig. 13 for both the gravity-driven and stress-driven problems. The unit of length is the half-width $\lambda/2$ of the mode of fastest finger growth in each case. For the particular wetting-layer thickness $\delta = 0.05$, the steady-state profile for the stress-driven profile is seen to be the longer of the two. The ratio of peak-to-trough finger length over the wavelength λ is 4.3 for the gravity case, compared with about 6.8 for the stress problem. The maximum thickness, at the bulbous front, is approximately the

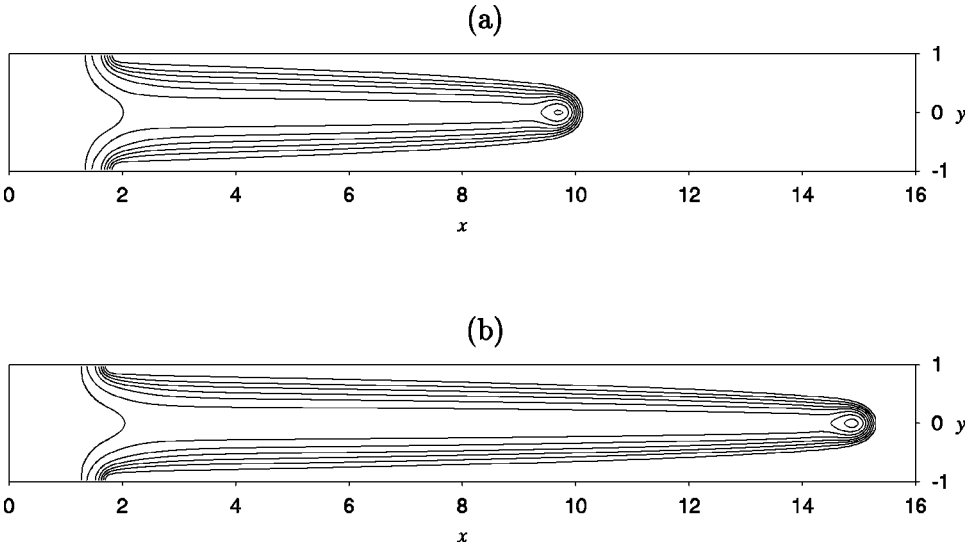

FIG. 13. Comparison of steady-state wedge-shaped fingers for (a) gravity-driven, and (b) surface-shear-stress-driven flow, assuming perfect wetting with $\delta=0.05$. One-half of a bilaterally symmetic finger is shown in each case. Here length dimensions are shown in units of the finger half-width. Contour line spacing is $\Delta h=0.20$. Case (b) is the predicted final shape of the finger examined experimentally in Fig. 11 if it were possible to extend the experimental domain indefinitely.

same for each of the cases and is about 1.5 times the upstream thickness.

The existence of steady-state profiles is not unexpected and was, in fact, observed in gravity drainage of thin liquid films on an inclined plate when the equilibrium contact angle θ_e was small.[15] Unlike the present problem, however, where liquid is supplied upstream at a constant rate, these experiments used a mound of liquid, initially held behind a dam, which was then released and allowed to flow downward. Because the two problems are not the same, only a qualitative comparison is possible.

A simple argument to justify the steady-state result follows from a ''slender body'' viewpoint. Consider a long slender finger whose cross-section changes slowly with distance in the streamwise direction. As the finger propagates downstream, it also spreads sideways. In any cross plane $x=$const, the finger profile is approximately parabolic and has a maximum inclination or apparent dynamic contact angle $\theta(t)$ in that plane. The sideways spreading will continue so long as $\theta(t)>\theta_e$. If θ_e is small enough, the finger will spread until its width equals the finger spacing λ. At this point, the finger ''trough'' is formed and the frontal profile is established. This three-dimensional profile will then propagate downstream as a single unit without further change of form. Conversely, for larger values of θ_e, it is possible that the sideways spreading will stop when the cross plane angle $\theta\approx\theta_e$ and that this will occur for finger widths less than λ. In this latter case, very long straight-sided fingers can be expected. In the same series of experiments[15] such long fingers were indeed observed when the substrate was replaced by one that exhibited a large value of θ_e for the liquid that was used.

Confirmation that steady states are established is provided by Fig. 14 where the integral norm $\|h_1\|$, defined in (28), is plotted versus time. For each of the two problems, $\|h_1\|$ clearly reaches a constant value after sufficient time has elapsed. Since $\|h_1\|$ depends only on the profile shape in a wave-fixed coordinate system, its constancy indicates that the profile is no longer changing.

The following figures illustrate modifications to the patterns arising from finite-contact-angle effects. Figures 15(a)–15(d) are contour plots of gravity-drainage fingers as the contact angle increases monotonically. All pictures correspond to the same time $t=360$ after the imposition of a small disturbance. None of the fingers has yet reached steady state at this time. As before, the plots are drawn in a moving coordinate system and $x=0$ is the location of the apparent

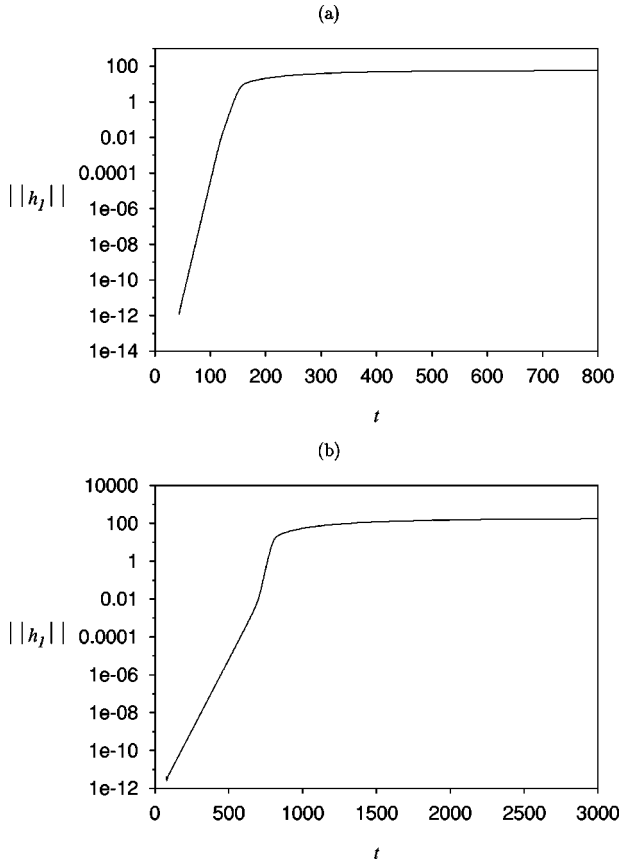

FIG. 14. Long-time behavior of an integral norm for (a) gravity-driven and (b) surface-shear-stress-driven flow problems. The norm becomes constant in each case, demonstrating that a steady-state propagating finger is formed. Here $\theta_e=0$, $\delta=0.05$.

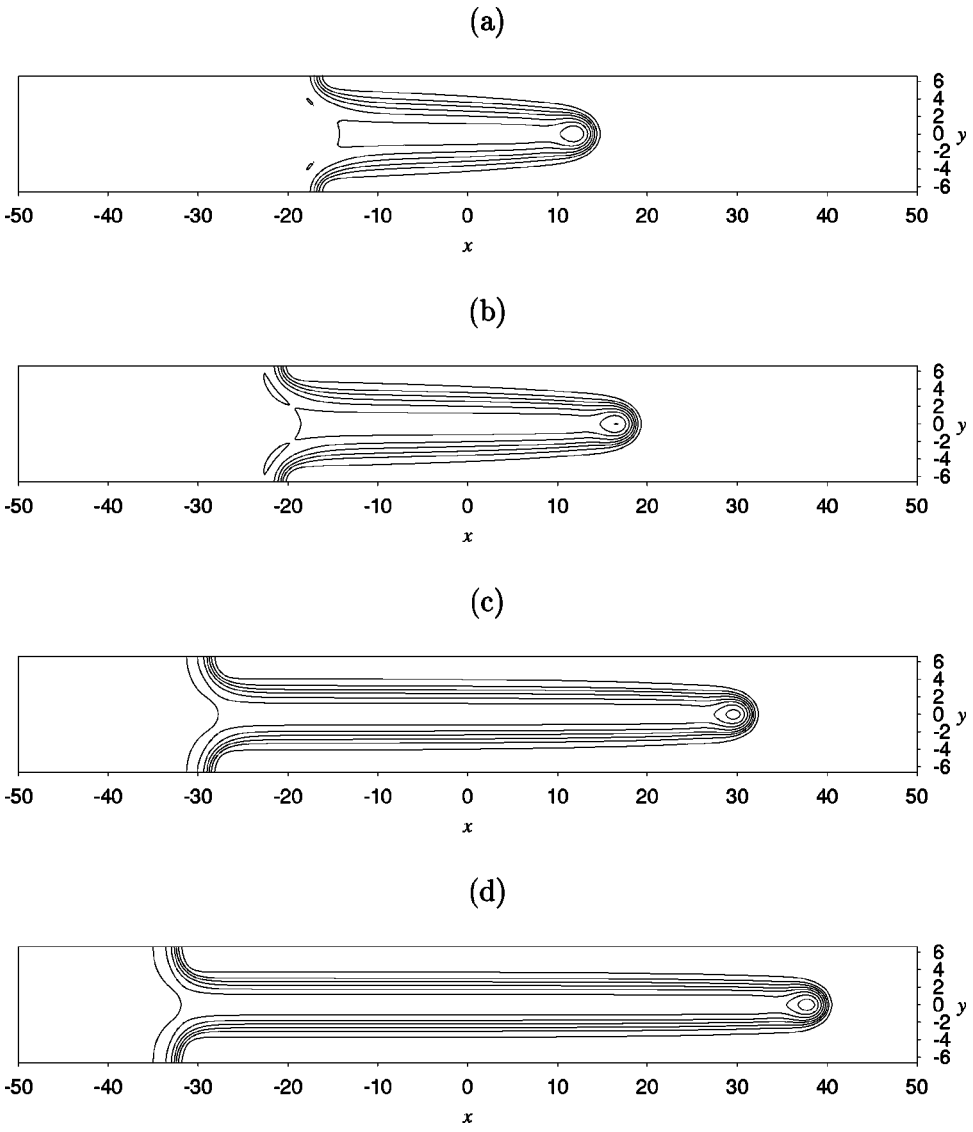

FIG. 15. Transition from wedge-shaped fingers to long rivulets as the equilibrium contact angle θ_e is increased. All profiles are shown at the same time, $t=360$, showing that fingers grow faster for larger θ_e. Gravity-driven flow; $\delta=0.1$. In the model $K\delta=\theta_e^2/(3\mathrm{Ca})^{2/3}$. The $K\delta$ values are (a) 0.1, (b) 0.25, (c) 0.5, and (d) 0.75. The contour line spacing is $\Delta h=0.20$. The exponents in the disjoining pressure functional are $(n,m)=(3,2)$.

contact line of the base state for each case. In all cases, finger tips move faster than the upstream flow speed while troughs move more slowly. The slip thickness is $\delta=0.1$ and the contour height intervals are 0.2 h_∞ in these plots while the contact angle parameter increases from $K=1$ to $K=7.5$. Note that $K\delta\propto\theta_e^2$. The trend as K increases is seen to be a transition from a relatively short wedge to long fingers with straight sides.

The set of calculations leading to Figs. 15(a)–15(d) was repeated using a disjoining exponent pair $(n,m)=(4,3)$. Results for two of the four values of contact angle are shown in Fig. 16. As expected, the effect of the change in disjoining exponents is greater when the contact angle θ_e is larger. For the two comparison cases shown, the difference in layer thickness with the fingers, resulting from the exponent change, is quite small; it is less than about 2%. The speeds of finger growth and the finger lengths at a given time are both somewhat larger for the (4,3) choice. The difference in finger lengths is seen to be about 4% for the smaller contact angle parameter (a) $K\delta=0.1$ and about 10% for (b) $K\delta=0.5$. Comparison of Figs. 15 and 16 demonstrates that dynamic behavior of systems that exhibit a finite static angle θ_e is controlled primarily by θ_e itself and that the details of the disjoining model is a secondary effect.

Figure 17 shows the behavior in time of the two integral norms, $E^{(\sigma)}-E_0^{(\sigma)}$ and $\|h_1\|$, for each of the contact-angle parameter values used in Fig. 15. The calculations have been extended to times much greater than that of the ''snapshots'' in Fig. 15. The two integral norms behave similarly. For the smallest parameter value $K=1$, a constant value of each norm is ultimately attained indicating the finger growth has stopped and the profile then translates without further change of form. For a straight-sided long finger whose length is increasing at a constant rate and whose tip and trough have an invariant form, the plot of either norm versus time should be a straight line. This seems to be the case for the two largest values of K. The slope of these lines is indicative of the rate at which the finger length is increasing. Thus the $K=7.5$ finger is elongating more rapidly than the $K=5$ finger. The intermediate case $K=2.5$ also appears as if it will stabilize yielding a final finger of finite length. Because of the quadratic dependence of K on θ_e, the static contact angle for the largest K value is only about 2.74 times larger than that angle for $K=1$. Qualitatively, therefore, relatively small con-

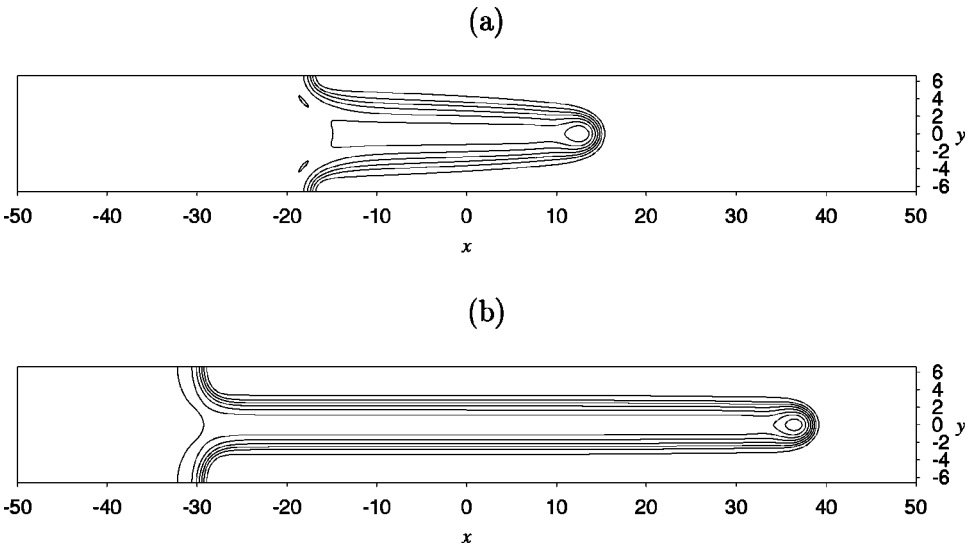

FIG. 16. The calculations of Fig. 15 are repeated using a different choice of disjoining exponents $(n,m)=(4,3)$. The contact angle parameters here are (a) $K\delta=0.1$ and (b) $K\delta=0.5$ corresponding to cases (a) and (c) in Fig. 15. All other parameter values are the same. The rate of finger growth is slightly larger using the (4,3) exponents.

tact angles will behave like perfectly wetting cases for which $\theta_e=0$, while larger values of θ_e will yield long fingers that grow at a constant rate. For a given set of input parameters, it should be possible to identify a critical value of θ_e at which this transition occurs. While not shown, the behavior of the closely related stress-driven problem is similar to the gravity case.

Rendered plots of two of the cases of gravity fingering are given in Fig. 18. Two periodic cycles are shown. The picture on the left is the small contact angle case corresponding to $K=1$. It has reached its final steady-state configuration, the actual dimensionless time is $t=3300$. The picture on the right is the $K=7.5$ case and shows long straight-sided fingers at a time $t=600$. Certain other interesting features of

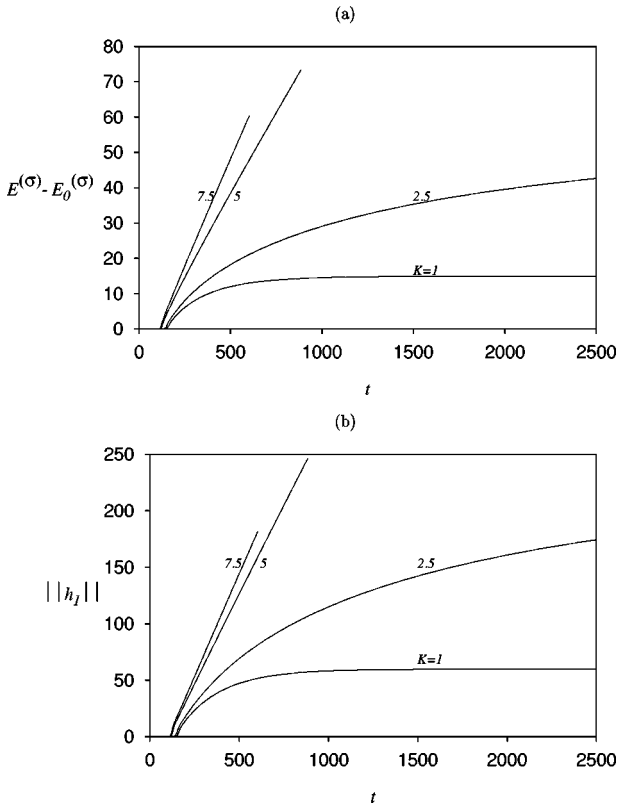

FIG. 17. Long-time behavior of two integral norms for gravity-driven flow. Straight lines indicates that the finger length is increasing at a constant rate. Values of the contact angle parameter K are the same as those in Fig. 15(a)–15(d). $\delta=0.1$.

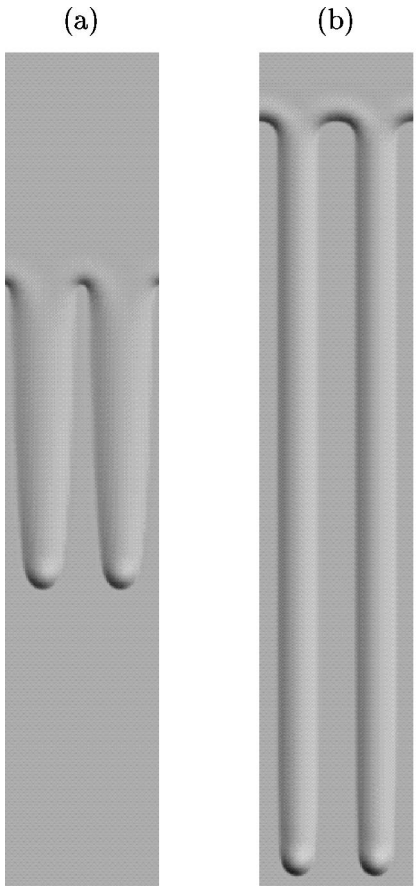

FIG. 18. Rendered pictures of fingers in gravity drainage. (a) Steady-state wedge-shaped fingers, with finger length=4λ, for $K\delta=0.1$. (b) Continually growing fingers for $K\delta=0.75$. The finger length is 10λ at $t=600$ for $K\delta=0.75$, as shown. Further elongation, at a constant rate, was calculated until the fingers were at least twice this length.

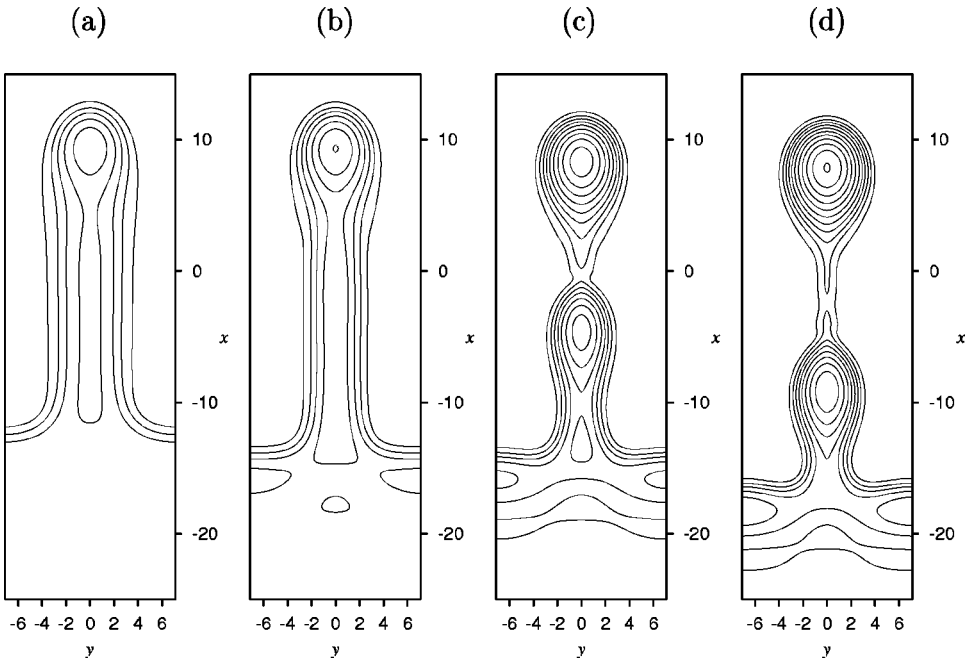

FIG. 19. Finger break up and droplet formation as the contact angle parameter is increased to large values. Shear-stress-driven flow. (a) $K\delta=1$, time $t=310$; (b) $K\delta=2$, $t=208$; (c) $K\delta=4$, $t=167$; and (d) $K\delta=5$, $t=135$. $\delta=0.1$. Contour line spacing is $\Delta h=0.40$. Fingers are drawn in a coordinate system that is moving at the base-state speed.

the fingers are also visible in the pictures. Note the bulbous finger tips and the arched capillary ridges at the troughs. The latter is especially pronounced for the high-contact-angle case. Recently published experimental photographs of such trough ridges show similar circular-arc-like shapes.[40]

The θ_e regime for which long straight-sided steadily growing fingers form also has an upper bound. This is illustrated in Fig. 19 where contour plots of finger shape are shown for moderate and large $K\delta$ values. The upwardly growing fingers that are shown correspond to the stress-driven problem, but qualitatively similar behavior will occur in the gravity case. As $K\delta$ increases from 1 to 5 in parts (a) through (d) of the figure, the profile changes from straight-sided to a fundamentally unsteady regime characterized by periodic droplet shedding. This comparison is done at times where the finger has advanced about the same amount in each case. Since, as previously noted, finger growth is accelerated by an increase θ_e, the times for these snapshots decrease as $K\delta$ increases.

A time series of pictures is shown in Fig. 20 in order to illustrate the dynamics of break-up and droplet formation. The sequence uses $K\delta=5$, the largest value used in Fig. 19. Because the contact angle is large, the formed finger is subject to an interfacial instability somewhat similar to the well-known Rayleigh ''sausage'' instability for liquid jets of initially circular cross section. For a *static* liquid mound or ridge with finite θ_e on a flat substrate, under the small slope assumption, the critical wavelength, i.e., the wavelength of neutral growth λ_N, has been calculated.[41] This static stability analysis has recently been extended to substrates of arbitrary shape and the restriction to small interface inclination and small contact angles has been removed.[42] It is remarkable that the more complete analysis validates the accuracy of the small-slope results for contact angles that are surprisingly large. Thus, for example, λ_N only changes by about 2% for a 45° contact angle. The present dynamic study has a number of features that are absent from the static analysis. Principal among these is the presence of flow in the growing finger.

It is useful to recognize the importance of contact angle and flow speed when considering the tendency of flowing fingers, or rivulets, to break up into a line of drops. From (12) and using the disjoining exponents $(n,m)=(3,2)$, the major dependence is

$$K\delta=\frac{\theta_e^2}{(3\mathrm{Ca})^{2/3}} \tag{31}$$

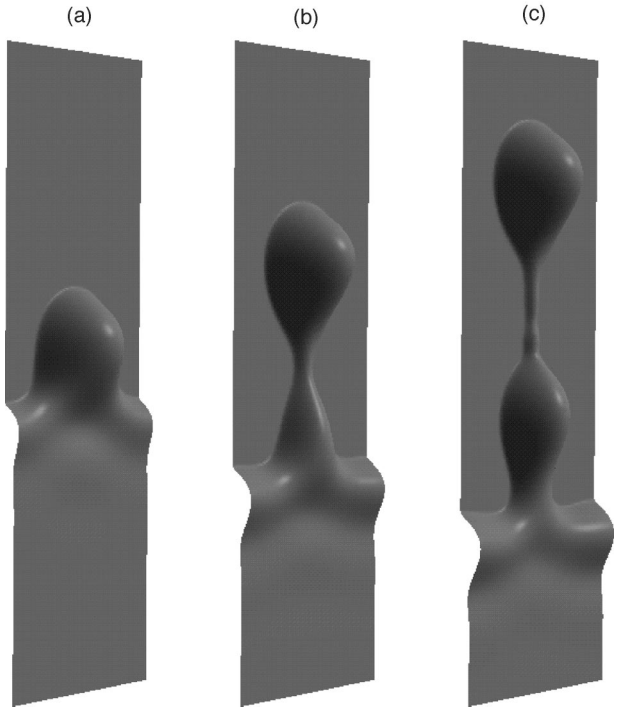

FIG. 20. A sequence of rendered pictures showing droplet formation. Stress-driven flow; $K\delta=5$. The times are (a) $t=118$, (b) $t=127$, and (c) $t=135$.

and the speed parameter Ca is formed from input quantities; for the stress-driven flow, the relation is $\mathrm{Ca}=\tau h_\infty/(2\sigma)$. Thus increasing the flow speed will tend to suppress finger beading for a given θ_e exactly as if the contact angle had been reduced instead. Maintenance of flow continuity in the slow flow of rivulets is potentially an issue of industrial importance. In addition to its effect on the finger spacing and overall speed of progression, increasing the driving stress τ, for a material system with a given θ_e, will tend to produce continuous patterns, such as Fig. 19(a) or 19(b), rather than droplet patterns in Fig. 19(c) or 19(d).

In the series of experiments of Cazabat *et al.*,[5,13] a typical set of parameter values is $\tau=1.8\,\mathrm{dyn/cm^2}$ and $\sigma=20\,\mathrm{dyn/cm}$. The capillary number is then 5×10^{-6} using Eq. (1). Because, in their experiments, silicone oil strongly wets the silicon wafer, θ_e can be expected to be quite small and flow patterns like Fig. 19(a) are produced. Had a different liquid or substrate been used instead, so that $\theta_e\approx3°$ say, then $K\delta\approx5$ and the patterns of Fig. 19(d), or Fig. 20, would result instead. Increasing τ by increasing the temperature gradient along the substrate will increase the flow speed and can be expected to retard or eliminate the tendency to break up the finger. Such an extended experimental program would provide a valuable comparison with the theoretical predictions given here.

A more immediate, albeit uncontrolled, observation of stress-driven fingering can be made while driving a car in a gentle rain. At a speed of about 40 miles per hour, without using windshield wipers, upwardly propagating horizontal waves with pronounced forward capillary ridges, driven by wind shear, can be observed on the windshield of a car. After moving a short distance, the ridges develop transverse oscillations that grow into fingers. The fingers have a width of about 2–3 mm and quickly grow to a length of at least 2 cm. The behavior is quite different for a windshield treated with Rain-X, a commercial product containing siloxanes. Under similar gentle-rain conditions, rather than form continuous fingers, each incipient finger sheds a chain of drops in a manner similar to the sequence in Fig. 20. In the laboratory we have measured static contact angles θ_e of $10°-15°$ for small water droplets on clean untreated glass. Depending on the number of coats applied, Rain-X treated glass exhibits θ_e values in the range $30°-50°$.

Periodic shedding of droplets for large values of $K\delta$ is confirmed by the time behavior of the two integral measures shown in Fig. 21. This simulation uses the value $K\delta=4$, corresponding to the picture in Fig. 19(c), and is calculated to somewhat larger times. The norm $\|h_1\|$ is seen to be the more sensitive of the two and indicates droplet formation events at $t\approx160$ and $t\approx180$. This periodic behavior will continue indefinitely.

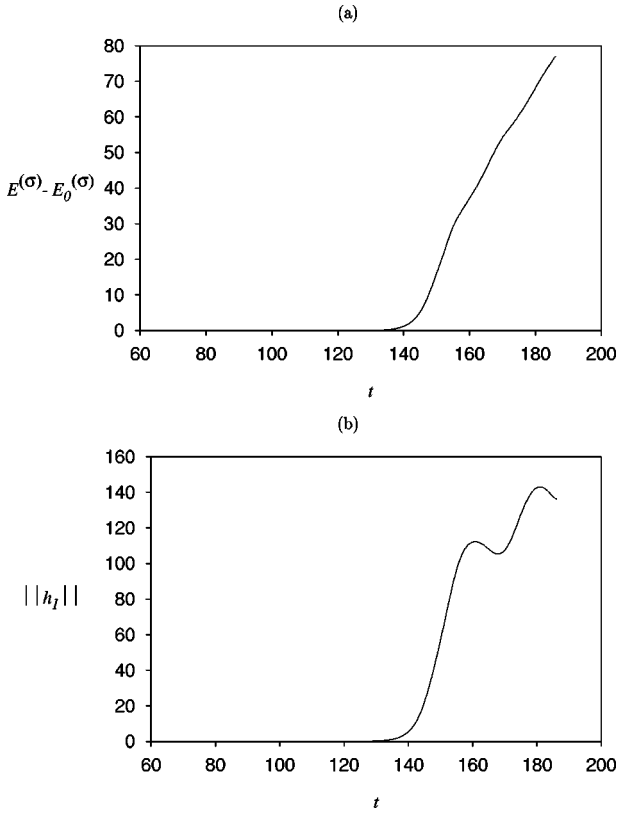

FIG. 21. Time evolution of two integral norms for the parameter values of Fig. 19(c). Slope changes in (a) and undulations in (b) indicate cyclical droplet shedding at this large contact angle.

IV. CONCLUDING REMARKS

In this study we have developed a mathematical model for flow in thin fluid layers including the influence of capillarity and dynamic contact angle effects. The flow is driven by gravity forces, an applied surface shear stress, or some combination of both effects. The numerical algorithm that is used to solve the model equations will calculate time-dependent three-dimensional motion starting from an arbitrary initial configuration. Dynamic contact line behavior arises naturally from interfacial energetic considerations. Because contact lines are captured by the algorithm, without the need for specific tracking of their positions, a highly efficient alternating-direction-implicit time marching algorithm can be used.

For definiteness, in the present work, consideration is restricted to two problems; each of these have a nontrivial base-state solution that is steady in a profile-fixed coordinate system. The liquid is assumed to be Newtonian and nonvolatile, the surface shear stress is constant, and the plane substrate is chemically and physically homogeneous. Each of these restrictions can be removed in a more general numerical model.[22,23,39,43,44]

When a base-state solution is sinusoidally perturbed in the transverse direction, a particular mode of fastest growth is selected that ultimately evolves into a nonlinear fingering pattern. At early times, while the perturbation is still small, the numerical algorithm shows an exponential rate of growth. All details of the early-time behavior, including wavelength selection, growth rate, and eigenmode, agree closely with published linear stability analyses.[11,12]

Under an assumption of perfect wetting, we have modeled the Marangoni-stress-driven flows in the experiments of Cazabat *et al.*[5,13] Finger shapes, as calculated, match the experimental interferographs and the time scales for finger de-

velopment and growth are also correctly predicted. A free parameter in the simulation is the unknown precursor layer thickness. A best fit to the experimental profile is a precursor layer that is about 20 nm in depth, which is a plausible value. Halving this thickness only changes the predicted profile by a small amount.

At large times, for perfect wetting, the fingers grow to a specific finite length in each of the two problems that have been considered. A limiting profile is calculated, for each problem, that translates without further change of form at a speed equal to the speed of the original base state. Such limiting wedge-shaped fingers are qualitatively similar to those observed experimentally.[14,15] These experiments are not directly comparable to the present simulation because they deal with the collapse of an initial mound rather than the evolution of a slightly perturbed base flow. The mound collapse problem was simulated some time ago using an early form of the present algorithm.[17]

Finite-contact-angle effects are reproduced using a model function with two essential free parameters. One of these is the static or equilibrium contact angle θ_e, a macroscopically observable physical quantity that depends only on the nature of the liquid and substrate. The second is the thickness of a thin energetically stable precursor layer that acts as a slip coefficient. The macroscopic finger or droplet edge meets this slip layer at an apparent contact line. Both advancing and receding contact line movement is possible with this so-called disjoining-pressure model. Two other parameters in the model, the exponents (n,m) in Eq. (6), control the dynamic change in contact angle. In most cases, an advancing contact angle will be larger than θ_e, while a receding angle will be smaller, in a slow, spontaneous, i.e., unforced, motion. No general relation between dynamic contact angle and contact-line speed is possible however, since neither of these quantities is determined solely by local conditions. These local quantities depend on remote effects such as the distribution of the driving forces in the flow field. Consistent with earlier work,[22,23] we have shown that other choices for (n,m) cause modest quantitative rather than qualitative changes in the evolving flow. The particular choice $(n,m)=(3,2)$ used for most of the calculations produces realistic flow behavior and appears to match available experimental data.

Depending on the size of the contact angle parameter, three distinct regimes are observed. For small but finite values, relatively short wedge-shaped fingers ultimately form; this pattern then translates at constant speed without further change of form. This regime can be thought of as an extension of the perfectly wetting, zero-contact-angle case and, in the final pattern, fingers are only modestly longer than those produced when $\theta_e=0$. For large angles, a second regime exists, where straight-sided fingers appear; they increase in length at a constant rate, apparently without limit. Finally, when the contact angle is larger still, there is a cyclical third regime. Here the incipient fingers periodically break up, leading to chains of isolated drops. Because the contact angle parameter includes an inverse dependence on flow speed, the transition from a continuously flowing finger to a broken pattern of drops is speed dependent. Specifically, the preservation of continuously flowing rivulets, a problem of importance in a number of applications, requires that a certain minimum flow rate be maintained. The numerical evidence is that well-defined critical values exist that separate these three distinct regimes. While the calculations were carefully done, and the numerical evidence is considered to be strong, no mathematically rigorous result, based perhaps on limit-point theory, has been devised.

Further work is required, both experimentally and theoretically, to strengthen and validate the model given here. While there is experimental and/or observational confirmation for each effect modeled here, relatively little quantitative data is available. Of particular value would be careful measurements, perhaps using interferometry, of the shape evolution of liquid fronts, with particular emphasis on the immediate neighborhood of the moving contact line, on well-characterized substrates. The numerical model is easily adapted to treat flow configurations that are different from those discussed here, so that various experimental configurations can be simulated. Of special interest would be new phenomena that may lead to modifications or corrections to the disjoining pressure functional in the model. For partially wetting systems, values of the slip thickness $\tilde{h}_*$ that can currently be used in the numerical model are larger than they should be. Algorithmic improvements are being pursued to allow computation with significantly smaller values of this quantity.

ACKNOWLEDGMENTS

This work is supported by the NASA Microgravity Program, the ICI Business Link Partnership, and the State of Delaware.

[1] D. Thoenes, *Chemical Reactor Development from Laboratory Synthesis to Industrial Production* (Kluwer Academic, Dordrecht, 1994).
[2] F. Kastanek, J. Zahradnik, J. Kratochvil, and J. Cermak, *Chemical Reactors for Gas-Liquid Systems* (Ellis Horwood, New York, 1993).
[3] L. H. Tanner, ''Les gouttes (the drops),'' Recherche **17**, 183 (1986).
[4] V. Ludviksson and E. N. Lightfoot, ''The dynamics of thin liquid films in the presence of surface-tension gradients,'' AIChE J. **17**, 1166 (1971).
[5] A. M. Cazabat, F. Heslot, P. Carles, and S. M. Troian, ''Hydrodynamic fingering instability of driven wetting films,'' Adv. Colloid Interface Sci. **39**, 61 (1992).
[6] P. Carles and A. M. Cazabat, ''The thickness of surface-tension-gradient-driven spreading films,'' J. Colloid Interface Sci. **157**, 196 (1993).
[7] X. Fanton, A. M. Cazabat, and D. Quere, ''Thickness and shape of films driven by Marangoni flow,'' Langmuir **12**(24), 5875 (1996).
[8] V. G. Levich, *Physiochemical Hydrodynamics* (Prentice-Hall, Englewood Cliffs, NJ, 1962).
[9] C. Huh and L. E. Scriven, ''Hydrodynamic model of steady movement of a solid/liquid/fluid contact line,'' J. Colloid Interface Sci. **35**, 85 (1971).
[10] E. O. Tuck and L. W. Schwartz, ''A numerical and asymptotic study of some third-order ordinary differential equations relevant to draining and coating flows,'' SIAM Rev. **32**(3), 453 (1990).
[11] D. E. Kataoka and S. M. Troian, ''A theoretical study of instabilities at the advancing front of thermally driven coating films,'' J. Colloid Interface Sci. **192**, 350 (1997).
[12] M. A. Spaid and G. M. Homsy, ''Stability of Newtonian and viscoelastic dynamic contact lines,'' Phys. Fluids **8**(2), 460 (1996).
[13] A. M. Cazabat, F. Heslot, S. M. Troian, and P. Carles, ''Fingering instability of thin spreading films driven by temperature gradients,'' Nature (London) **346**(6287), 824 (1990).
[14] H. E. Huppert, ''Flow and instability of a viscous current down a slope,'' Nature (London) **300**(5891), 427 (1982).

[15]N. Silvi and E. B. Dussan V., ''On the rewetting of an inclined solid surface by a liquid,'' Phys. Fluids **28**, 5 (1985).
[16]J. M. Jerrett and J. R. de Bruyn, ''Fingering instability of a gravitationally driven contact line,'' Phys. Fluids A **4**, 234 (1992).
[17]L. W. Schwartz, ''Viscous flows down an inclined plane: Instability and finger formation,'' Phys. Fluids A **1**, 443 (1989).
[18]S. T. Thoroddsen and L. Mahadevan, ''Experimental study of coating flows in a partially-filled horizontally rotating cylinder,'' Exp. Fluids **23**, 1 (1997).
[19]A. E. Hosoi and L. Mahadevan, ''Axial instability of a free-surface front in a partially filled horizontal rotating cylinder,'' Phys. Fluids **11**, 97 (1999).
[20]A. T. Jameel and A. Sharma, ''Morphological phase separation in thin liquid films. II. Equilibrium contact angles of nanodrops coexisting with thin films,'' J. Colloid Interface Sci. **164**, 416 (1994).
[21]V. S. Mitlin and N. V. Petviashvili, ''Nonlinear dynamics of dewetting: Kinetically stable structures,'' Phys. Lett. A **192**, 323 (1994).
[22]L. W. Schwartz, ''Hysteretic effects in droplet motions on heterogeneous substrates: Direct numerical simulation,'' Langmuir **14**, 3440 (1998).
[23]L. W. Schwartz and R. R. Eley, ''Simulation of droplet motion on low-energy and heterogeneous surfaces,'' J. Colloid Interface Sci. **202**, 173 (1998).
[24]D. J. Benney, ''Long waves on liquid films,'' J. Math. Phys., **45**, 150 (1966).
[25]R. W. Atherton and G. M. Homsy, ''On the derivation of evolution equations for interfacial waves,'' Chem. Eng. Commun. **2**, 57 (1976).
[26]A. N. Frumkin, ''On the phenomena of wetting and sticking of bubbles,'' Zh. Fiz. Khim. **12**, 337 (1938) (in Russian).
[27]B. V. Derjaguin, ''Theory of the capillary condensation and other capillary phenomena taking into account the disjoining effect of long-chain molecular liquid films,'' Zh. Fiz. Khim. **14**, 137 (1940) (in Russian).
[28]G. F. Teletzke, H. T. Davis, and L. E. Scriven, ''How liquids spread on solids,'' Chem. Eng. Commun. **55**, 41 (1987).
[29]M. B. Williams and S. H. Davis, ''Nonlinear theory of film rupture,'' J. Colloid Interface Sci. **90**, 220 (1982).
[30]H. S. Kheshgi and L. E. Scriven, ''Dewetting—Nucleation and growth of dry regions,'' Chem. Eng. Sci. **46**, 519 (1991).
[31]P. G. De Gennes, ''Wetting: statics and dynamics,'' Rev. Mod. Phys. **57**, 827 (1985).
[32]G. F. Teletzke, H. T. Davis, and L. E. Scriven, ''Wetting hydrodynamics,'' Rev. Phys. Appl. **23**, 989 (1988).
[33]H. P. Greenspan, ''On the motion of a small viscous droplet that wets a surface,'' J. Fluid Mech. **84**, 125 (1978).
[34]D. T. Moyle, M. S. Chen, and G. M. Homsy, ''Nonlinear rivulet dynamics during unstable dynamic wetting flows,'' Int. J. Multiphase Flow **25**, 1243 (1999).
[35]D. W. Peaceman and H. H. Rachford, Jr., ''The numerical solution of parabolic and elliptic differential equations,'' J. Soc. Ind. Appl. Math. **3**, 28 (1955).
[36]S. D. Conte and R. T. Dames, ''An alternating direction method for solving the biharmonic equation,'' Math. Tables Aids Com. **12**, 198 (1958).
[37]N. N. Yanenko, *The Method of Fractional Steps* (Springer-Verlag, New York, 1971).
[38]J. A. Moriarty and L. W. Schwartz, ''Dynamic considerations in the closing and opening of holes in thin liquid films,'' J. Colloid Interface Sci. **161**, 335 (1993).
[39]D. E. Weidner, L. W. Schwartz, and M. H. Eres, ''Simulation of coating layer evolution and drop formation on horizontal cylinders,'' J. Colloid Interface Sci. **187a**, 243 (1997).
[40]T. Podgorski, J. M. Flesselles, and L. Limat, ''Dry arches within flowing films,'' Phys. Fluids **11**, 845 (1999).
[41]K. Sekimoto, R. Oguma, and K. Kawazaki, ''Morphological stability analysis of partial wetting,'' Ann. Phys. (N.Y.) **176**, 359–392 (1987).
[42]R. V. Roy and L. W. Schwartz, ''On the stability of liquid ridges,'' J. Fluid Mech. **391**, 293–318 (1999).
[43]M. H. Eres, D. E. Weidner, and L. W. Schwartz, ''Three-dimensional direct numerical simulation of surface-tension-gradient effects on the leveling of an evaporating multicomponent fluid,'' Langmuir **15**, 1859–1871 (1999).
[44]L. W. Schwartz, P. Moussalli, P. Campbell, and R. R. Eley, ''Numerical modelling of liquid withdrawal from gravure cavities in coating operations,'' Trans. Inst. Chem. Eng. **76**, 22–29 (1998).